# Unified Modeling and Analysis of Dynamic Power Coupling for Grid-Forming Converters

Mingxuan Li, *Member, IEEE*, Yue Wang, *Member, IEEE*, Weihao Hu, *Senior Member, IEEE*, Sirui Shu, Peng Yu, Zhenyuan Zhang, *Senior Member, IEEE*, and Frede Blaabjerg, *Fellow, IEEE*

***Abstract*—Grid-forming converters, taking droop-controlled converters and virtual synchronous generators (VSGs) as typical examples, have shown great promise as the interfaces between renewable energy sources and the future power-electronics-based power system. However, the coupling between active and reactive power will adversely affect the dynamic performance and stability of grid-forming converters. In order to facilitate quantitatively analyzing and assessing the power coupling characteristics of various types of grid-forming strategies, this article develops a unified dynamic power coupling model based on a first amplification coefficient array and a relative gain array in the frequency domain. Then, by using the established unified model, a comprehensive analysis of dynamic power coupling properties for typical VSG control and droop control is presented, which reveals that droop control is helpful in weakening power coupling while VSG control is prone to amplify the coupling. Moreover, the influences of the pivotal control parameters in droop and VSG controllers on power coupling characteristics are discussed in detail, which can provide novel supplementary guidelines for parameter design of droop and VSG controllers. Finally, the experimental results verify the correctness of theoretical modeling and analysis.**

***Index Terms*—Droop control, grid-forming control, grid-forming converter, power coupling, power oscillation, virtual synchronous generator.**

## NOMENCLATURE

| | |
|---|---|
| $P$, $Q$ | Active power and reactive power output. |
| $P_{\rm ref}$, $Q_{\rm ref}$ | Active power and reactive power reference. |
| $\omega$ | Angular frequency. |
| $\omega_0$, $\omega_{\rm ref}$ | Nominal angular frequency. |
| $J$ | Virtual inertia of VSG. |
| $k_{\rm P}$ | Active power droop coefficient or damping factor. |
| $k_{\rm Q}$ | Reactive power droop coefficient. |
| $E$, $\theta$ | Voltage rms value and phase of converter. |
| $E_{\rm ref}$ | Voltage rms value reference of converter. |
| $U$ | Ac bus voltage. |
| $R$, $X$ | Equivalent connected resistance and reactance. |
| $\delta$ | Power angle. |
| $\boldsymbol{u}$ | Manipulated variable vector. |
| $\boldsymbol{y}$ | Controlled variable vector. |
| $\mathbf{P}$ | First amplification coefficient array. |
| $\mathbf{\Lambda}$ | Relative gain array. |
| const | Constant value. |
| $s$ | Complex operator/Laplace variable. |
| $\angle$ | Phase of complex variable. |
| $\lvert\cdot\rvert$, abs | Modulus of complex variable. |
| $\Delta$ | Disturbance of a variable. |

*Superscript:*

| | |
|---|---|
| F, D, V | Variables related to power flow, droop control system and VSG system. |
| $-1$, T | Inverse and transposition of matrix. |
| $s\to\infty$, $s\to0$ | The limits at the point $s=\infty$ and $s=0$. |
| $\omega\to\infty$, $\omega\to0$ | The limits at the point $\omega=\infty$ and $\omega=0$. |

*Subscripts:*

| | |
|---|---|
| 0 | Values in steady-state condition. |
| ref | Reference value. |
| P, Q | Variables related to active power loop and reactive power loop. |
| $i$, $j$ | Row number and column number of a matrix or array. |

*Abbreviation*

| | |
|---|---|
| VSG | Virtual synchronous generator. |
| SG | Synchronous generator. |
| FAA | First amplification coefficient array. |
| RGA | Relative gain array. |

Manuscript received March 14, 2021; revised June 22, 2021; accepted August 9, 2021. Date of publication August 24, 2021; date of current version October 15, 2021. This work was supported by the National Natural Science Foundation of China under Grant 51777159. Recommended for publication by Associate Editor M. Su. *(Corresponding author: Yue Wang.)*

Mingxuan Li is with the School of Electrical Engineering, Xi'an Jiaotong University, Xi'an 710049, China, and also with the School of Mechanical and Electrical Engineering, University of Electronic Science and Technology of China, Chengdu 611731, China (e-mail: lmxzyqt@126.com).

Yue Wang, Sirui Shu, and Peng Yu are with the School of Electrical Engineering, Xi'an Jiaotong University, Xi'an 710049, China (e-mail: davidwangyue@mail.xjtu.edu.cn; ssr5dd@stu.xjtu.edu.cn; tinyfish0203@stu.xjtu.edu.cn).

Weihao Hu and Zhenyuan Zhang are with the School of Mechanical and Electrical Engineering, University of Electronic Science and Technology of China, Chengdu 611731, China (e-mail: whu@uestc.edu.cn; zhangzhenyuan@uestc.edu.cn).

Frede Blaabjerg is with the Department of Energy Technology, Aalborg University, 9220 Aalborg, Denmark (e-mail: fbl@et.aau.dk).

Color versions of one or more figures in this article are available at https://doi.org/10.1109/TPEL.2021.3107329.

Digital Object Identifier 10.1109/TPEL.2021.3107329

## I. INTRODUCTION

RENEWABLE energy sources (RES) mostly interface with the power grid by using grid-connected converters [1], [2].

A variety of control strategies have been proposed to equip the grid-connected converters with different functions and external response performance [3], [4]. Generally, the control strategies of grid-connected converters can be divided into two categories [4]–[7]. The first category is grid-following converter [7], also called grid-feeding converter in some publications [4], which is controlled as a current source to feed power into the grid. Grid-following converters have been the most widely used ways in the past decades because of their advantages, including simplification of implementation, suitability for parallel operation, ability of tracking the maximum power point, etc. However, the grid-following converters lack grid-forming ability by themselves, and have to depend on the support of the other voltage sources, which will aggravate frequency problems and cannot be adapted to the current trend towards power-electronics-dominated power grid [7]–[10].

Another category is grid-forming converter, which works as a voltage source with a given amplitude and frequency [9]. Compared to grid-following converter, grid-forming converters can provide voltage by themselves. To achieve parallel operation of multiple grid-forming converters and provide the grid with auxiliary services, inspired by the primary control in synchronous generators (SGs), two types of grid-forming control strategies, namely droop control [11] and virtual synchronous generator (VSG) control [12]–[14] are proposed in succession. The fundamental difference between droop control and VSG control is that the latter adds virtual inertia in further by mimicking the swing equation of SGs. Furthermore, in order to improve the performance of grid-forming converters, diverse variants of droop control and VSG control have also been proposed [15]–[24], which also belong to the grid-forming control family. Grid-forming control has become a promising technology because it can achieve the large-scale access to the grid and is more suitable for the power-electronics-dominated and decentralized paradigm of future power systems [9], [25].

The basic idea of a grid-forming converter is to control the active power and reactive power delivered to the grid by regulating the voltage amplitude and frequency (phase) of a grid-connected converter. The foundation of grid-forming control is the decoupling characteristics of power flow through transmission line, i.e., for the circumstances of a small power angle and purely inductive impedance between two voltage sources, the active power depends predominantly on power angle (integral of frequency), whereas the reactive power depends predominantly on voltage amplitude [11], [26]. Thus, by adjusting the frequency and amplitude of output voltage of a converter independently, the active power and reactive power are determined respectively, and vice versa. However, the two fundamental preconditions, i.e., small power angle and purely inductive impedance, are generally not satisfied under many circumstances. As a result, the unwanted cross coupling between the manipulated variables, viz. frequency and amplitude of output voltage, and the controlled output variables, viz. active power and reactive power fed into the transmission line, will be produced, which will make the abovementioned independent control law become no longer valid and would further cause the deterioration in the dynamic performance and stability of grid-forming converters [26], [27].

To tackle power coupling problems, many power decoupling methods for droop-based converters have been proposed over the past decade, which mainly includes virtual impedance method [28], [29], virtual power method [26], [30], [31], virtual frequency and voltage method [32], and power feedforward compensation method [33]. These methods provide effective solutions to deal with the power coupling caused by the high line impedance ratio $R/X$ in the low-voltage networks, but there still exist several problems to be addressed carefully. Especially, as a growing number of types of grid-forming strategies begin to emerge and become popular nowadays, e.g., VSG control, etc., much severer and more complicated power coupling problems have been created.

As mentioned previously, the unwanted power coupling in the power flow has an adverse impact on the performance and stability of grid-forming control strategies. On the other hand, different grid-forming control schemes and the corresponding parameters inside will affect power coupling of the whole system in turn, which is seldomly discussed in literature. Practically, even when the power flow has the same level of power coupling, different grid-forming converters can still exhibit quite distinct power coupling dynamic characteristics. In addition, the previous research perspectives are mainly confined to the static power coupling, however, very little research focuses on the dynamic coupling. The static coupling only considers the coupling correlation when the system is at steady state. Whereas, the dynamic coupling refers to the coupling issues during the whole dynamic process, including both the transient process and the final steady state. Actually, the dynamic coupling plays a more important role in dynamic performance and system stability because it can make a potential oscillation transmit between the active power loop and reactive power loop. Furthermore, the small power angle assumption error issue is always ignored in the previous methods, which also commonly exerts an important influence on power coupling. For example, phenomena of severe power coupling, resulting in a transient reactive power oscillation, a steady-state error and even instability, have been still observed even though the output impedance of VSG is purely inductive [34]–[36]. Therefore, the neglect of power angle issue is not reasonable any longer but should be taken into the model carefully. Recently, some researches on more accurate power coupling mechanism analysis and decoupling control strategies have been conducted, but they all only focus on one specific control structure and cannot adapt to the other grid-forming strategies [37], [38].

For the abovementioned reasons, it is necessary to reveal the dynamic power coupling characteristics and mechanism of various types of grid-forming converters more thoroughly. Unfortunately, there is still a lack of general accurate quantitative analysis models to give greater insights into the dynamic power coupling issues of grid-forming converters. Although the traditional small-signal models can be established to analyze the dynamic performance and stability of grid-forming converters, e.g., the state space model built in [6], [22], and [39], the dynamic phasor model built in [40], the reduced-order transfer function model built in [41], they cannot provide a specialized mathematical tool for analyzing the cross-coupling characteristics and

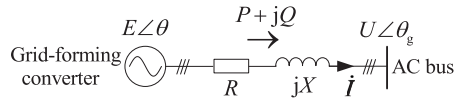


Fig. 1 Equivalent circuit of a grid-forming converter connected to an ac bus.

fail to give a deep-going and unified quantitative analysis of the power coupling characteristics of different grid-forming control strategies. The impedance-based and the harmonic state space based modeling methods are also investigated to analyze the grid-forming converters, e.g., the sequence impedance model built in [42], the impedance circuit model proposed in [43], the harmonic transfer function model in the frequency domain analyzed in [44], where the cross-coupling effects caused by the frame transformations and the frequency-coupling effects in the inner loops are well discussed. However, these models are still difficult to reveal the cross-coupling mechanisms between the active power and reactive power of the outer grid-forming control loops. To sum up, the abovementioned modeling methods are not perceptive enough to discover and analyze the more profound rules and latent problems on power dynamic coupling.

Motivated by the abovementioned problems, an in-depth research on the modeling and analysis of dynamic power coupling for grid-forming converters are conducted in this article. Compared to the previous research, the main contributions of this article are: first, a unified dynamic power coupling analysis model for grid-forming converters is proposed, which provides a universal quantitative analysis tool to assess power coupling of the whole control system for diverse grid-forming strategies; second, based on the proposed model, the effects of VSG and droop control on coupling characteristics are analyzed selectively, which reveals the differences of power coupling properties between VSG and droop control; third, the influences of the pivotal control parameters are discussed in detail, which can provide guidelines for parameter design of the droop and VSG controllers.

The rest of this article is organized as follows. In Section II, the grid-forming control strategies are briefly reviewed. In Section III, a universal dynamic power coupling model of grid-forming converters is built based on relative gain array (RGA) theory. In Section IV, power coupling properties of VSG and droop control are analyzed, and the effects of the pivotal control parameters are discussed. The experiment results are shown in Section V. Finally, Section VI concludes this article.

## II. Review of Grid-Forming Control Strategies

For a three-phase ac system with given distribution line impedances, illustrated in Fig. 1, the active and reactive power flowing between grid-forming converter and ac bus can be mathematically expressed as [28]

$$P = 3EI_c \sin\gamma_c - 3RI_c^2 \tag{1}$$

$$Q = 3EI_c \cos\gamma_c - 3XI_c^2 \tag{2}$$

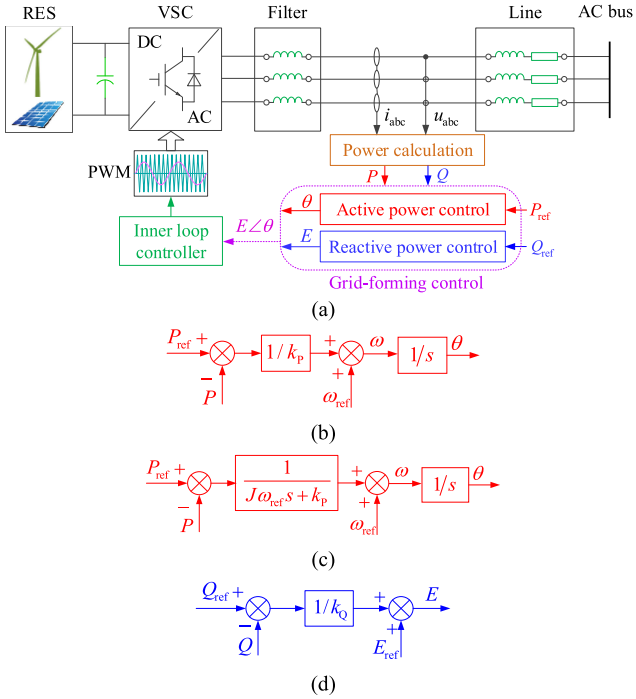


Fig. 2 General structure of a grid-forming converter. (a) Complete system. (b) Active control structure of typical droop control. (c) Active power structure of typical VSG control. (d) Reactive power droop control structure.

where $\gamma_c = \delta + \arctan(R/X)$, $\delta = \theta - \theta_g$, $I_c = U/\sqrt{R^2+X^2}$, $R$ and $X$ are equivalent connected resistance and reactance, respectively.

Considering that the equivalent connection impedance is mainly inductive, which is often justified by the high inductive components in filter-inductor and high-voltage or medium-voltage transmission line, and the power angle $\delta$ is usually quite small, (1) and (2) can be, respectively, simplified to

$$P = \frac{3EU}{X}\delta \tag{3}$$

$$Q = \frac{3(E-U)U}{X}. \tag{4}$$

The decoupling relationships described in (3) and (4) lay the foundation of grid-forming control, namely the output active power and reactive power can be realized by regulating the phase/frequency and magnitude of DG source, respectively.

The general structure of a grid-forming converter is depicted in Fig. 2(a). The power controller of grid-forming converter tracks the active and reactive power command and generates the magnitude and frequency (or phase) of the output voltage reference. The inner loop is employed to obtain better regulation ability of output voltage and current. The power controller can employ any types of grid-forming control strategies, as introduced in Section I.

The most widely used grid-forming controllers are typical droop and VSG control, whose active power controllers are

illustrated in Fig. 2(b) and (c) and mathematically described by

$$\omega = \omega_{\rm ref} + \frac{1}{k_{\rm P}}\left(P_{\rm ref} - P\right) \tag{5}$$

$$\omega = \omega_{\rm ref} + \frac{1}{J\omega_{\rm ref}s + k_{\rm P}}\left(P_{\rm ref} - P\right) \tag{6}$$

where $k_{\rm P}$ has two physical meanings, namely active power droop coefficient similar to droop control and damping factor indicated commonly by "*D*" in the other literature. Essentially, the two coefficients play the same role in the control loop and can be treated as one variable. For the convenience of analyzing VSG and droop control together, $k_{\rm P}$ is selected as a unified variable name in this article.

Furthermore, they employ a common reactive power droop controller, as illustrated in Fig. 2(d), and expressed as

$$E = E_{\rm ref} + \frac{1}{k_{\rm Q}}\left(Q_{\rm ref} - Q\right). \tag{7}$$

Actually, there are still many other kinds of grid-forming active power and reactive power controllers with different control structures and mathematical expressions, which will be introduced and summarized briefly in the latter sections. For lack of space, here only depicts the control structures that will be researched in detail later, and the others can be obtained by the open-loop functions listed subsequently.

As mentioned previously, the foundation that grid-forming control can work properly is the decoupling characteristics of power flowing through transmission line, which needs to satisfy two conditions, namely purely inductive line impedance and very small power angle. Actually, the two conditions are generally not satisfied, especially for low-voltage networks, high output impedance, etc. In these cases, (1) and (2) cannot be simplified to (3) and (4) any more.

Linearizing (1) and (2) at some initial steady-state points yield

$$\Delta P = 3E_0 I_{\rm c}\cos\gamma_{\rm c0}\Delta\delta + 3I_{\rm c}\sin\gamma_{\rm c0}\Delta E \tag{8}$$

$$\Delta Q = -3E_0 I_{\rm c}\sin\gamma_{\rm c0}\Delta\delta + 3I_{\rm c}\cos\gamma_{\rm c0}\Delta E \tag{9}$$

where $E_0$ is the steady-state inner voltage; $\gamma_{\rm c0} = \delta_0 + \arctan(R/X)$, $\delta_0$ is the power angle at initial steady-state point.

Expressions (8) and (9) indicate that when $\gamma_{\rm c0} \neq 0$, which is satisfied in almost all the cases, both active power and reactive power are functions of power angle and voltage magnitude. That is to say, active power and reactive power are coupled with each other rather than mutually independent. Consequently, the active power and reactive power control would interact and, thus, the performance and stability of grid-forming control strategies would deteriorate.

## III. Unified Dynamic Power Coupling Model of Grid-Forming Converters

### A. RGA Theory

In order to obtain a comprehensive understanding of coupling characteristics, RGA analysis method is employed in this article, which is an effective quantitative analysis tool of coupling degree for a multiple input multiple output (MIMO) system proposed by Bristol [45]. The principle of RGA is described briefly as follows.

Assuming $y_i$ is the *i*th controlled variable of a MIMO system and $u_j$ is the *j*th manipulated variable, the relative gain of the $u_j$–$y_i$ channel is defined as the ratio of the first amplification factor $p_{ij}$, and the second amplification factor $q_{ij}$, where $p_{ij}$ is the $u_j$–$y_i$ channel gain with other channels open and $q_{ij}$ is the $u_j$–$y_i$ channel gain with other channels closed and other controlled variables constant. The mathematical expression can be written as

$$\lambda_{ij} = \frac{p_{ij}}{q_{ij}} = \left.\frac{\partial y_i}{\partial u_j}\right|_{\substack{u_k=\text{const}\\(k\neq j)}} \Big/ \left.\frac{\partial y_i}{\partial u_j}\right|_{\substack{y_k=\text{const}\\(k\neq i)}}. \tag{10}$$

Arranging $p_{ij}$ in the order marked in subscript can construct the corresponding first amplification coefficient (FAA) **P**, and in similar way, arranging $\lambda_{ij}$ can yield RGA **Λ**. RGA describes the coupling relationship and coupling degree of a MIMO system. Practically, RGA can be calculated by FFA **P** directly

$$\mathbf{\Lambda} = \mathbf{P} \otimes \left(\mathbf{P}^{-1}\right)^{\rm T} \tag{11}$$

where $\otimes$ represents multiplication of the elements in the same place of matrixes.

To facilitate understanding the relationship and differences between FAA and RGA, some mathematical interpretations to (11) are given here. The elementwise product of **P**, indicating the transfer function matrix from $\boldsymbol{u}$ to $\boldsymbol{y}$, and $\mathbf{P}^{-1}$, indicating the inverse transfer function matrix from $\boldsymbol{y}$ to $\boldsymbol{u}$, makes **Λ** become dimensionless and, therefore, independent against the units of $\boldsymbol{u}$ and $\boldsymbol{y}$. On the contrary, **P** is not independent against units and, therefore, not neutral. Accordingly, **Λ** can give a unified and consistent evaluation criterion for coupling level regardless of the particular structures and parameters, while **P** cannot. Therefore, RGA can be used as a universal quantitative analysis tool for power coupling characteristics that can apply to all types of grid-forming converters. Based on this tool, comparative analysis can be conducted more simply even though when the research objects take different forms and thus novel conclusions can be discovered more probably, which is beyond the abilities of FAA. This is the chief advantage of RGA compared to FAA and thereby is the motivation of using **Λ** instead of **P** to evaluate the cross-coupling level.

The nondimensionalization of RGA also make RGA have such an important property: the sum of the elements of any row or column is 1. Using this characteristic of relative gain, the calculation of RGA can be further simplified.

Taking the object studied in this article as an example, a grid-forming control system can be regarded as a two-input-two-output system. Only the first amplification factor $p_{ij}$ is needed to find $\lambda_{11}$, and then each element of the entire RGA can be obtained.

RGA can be understood as a per-unit value of the coupling relationship of variables in a multivariable coupling system. In this way, all coupling systems can obtain the corresponding RGA and use the same coupling degree determination method to quantify the coupling degree of the system. The coupling

characteristics and variable pairing relationships reflected by the relative gain are summarized as follows [46].

1) When $\lambda_{11}=1$, the second channel has no coupling effect on the first channel. Opening or closing the second channel loop will not affect the first channel loop, so the pairing of $y_1$ and $u_1$ is the most suitable.
2) When $\lambda_{11}=0$, it indicates that $u_1$ does not have any control effect on $y_1$. In this case, $u_1$ and $y_1$ cannot be paired.
3) When $0<\lambda_{11}<1$, the second channel and the first channel have different degrees of coupling. Especially when $\lambda_{11}=0.5$, it indicates that there is the same coupling between the two channels. In this case, no matter how the variables are paired, the coupling between the two channels cannot be removed, so decoupling is necessary.
4) When $\lambda_{11}>1$, closing the second channel will reduce the gain between $y_1$ and $u_1$, indicating that there is a coupling between the channels. As $\lambda_{11}$ increases, the degree of coupling increases accordingly. When $\lambda_{11}$ is oversized, it is impossible to control the two output variables independently.
5) When $\lambda_{11}<0$, the opening or closing of the second channel will have the opposite effect on $y_1$, and the two control channels will be related in an incompatible manner. Therefore, $y_1$ should not be paired with $u_1$, otherwise, the closed-loop system may become unstable.

Therefore, this can be generalized to a recommended conclusion: when a controlled variable is paired with a manipulated variable, the corresponding relative gain must be as close to 1 as possible.

Without regard to grid-forming control, FFA for power flow equations can be obtained directly from (8) and (9), namely

$$\mathbf{P}^{\mathrm{F}}=\begin{bmatrix}K_{\mathrm{P}\delta} & K_{\mathrm{PE}}\\ K_{\mathrm{Q}\delta} & K_{\mathrm{QE}}\end{bmatrix}=\begin{bmatrix}3E_0I_{\mathrm{c}}\cos\gamma_{\mathrm{c}} & 3I_{\mathrm{c}}\sin\gamma_{\mathrm{c}}\\ -3E_0I_{\mathrm{c}}\sin\gamma_{\mathrm{c}} & 3I_{\mathrm{c}}\cos\gamma_{\mathrm{c}}\end{bmatrix}. \quad (12)$$

The corresponding RGA can be derived as

$$\mathbf{\Lambda}^{\mathrm{F}}=\begin{bmatrix}\lambda_{11}^{\mathrm{F}} & \lambda_{12}^{\mathrm{F}}\\ \lambda_{21}^{\mathrm{F}} & \lambda_{22}^{\mathrm{F}}\end{bmatrix}=\begin{bmatrix}\cos^2\gamma_{\mathrm{c}} & \sin^2\gamma_{\mathrm{c}}\\ \sin^2\gamma_{\mathrm{c}} & \cos^2\gamma_{\mathrm{c}}\end{bmatrix}. \quad (13)$$

It can be concluded that the coupling level in power flow is related to the power angle $\delta$ and line impedance ratio *R/X*. With the rise of $\delta$ and *R/X*, $\lambda_{11}^{\mathrm{F}}$ becomes smaller and moves away from 1, indicating a higher coupling level [27]. The significant impacts on the power coupling of $\delta$ and *R/X* have been investigated by the previous literature, e.g., [27], [30]. Thus, this article will further take the effects of the control structure and the parameters inside into account to research the dynamic power coupling issue of grid-forming converters.

### *B. Unified Dynamic Power Coupling Model of Grid-Forming Converter*

To analyze the power coupling properties including grid-forming control strategies, a unified dynamic coupling model of a grid-forming converter connected to power grid is established, as illustrated in Fig. 3, where $G_{\mathrm{c\_}\delta\mathrm{P}}(s)$ and $G_{\mathrm{c\_EQ}}(s)$ denote the equivalent open loop transfer functions of active power controller and reactive power controller, respectively, $G_{\mathrm{P}\delta}(s)$, $G_{\mathrm{PE}}(s)$, $G_{\mathrm{Q}\delta}(s)$, and $G_{\mathrm{QE}}(s)$ are the gains of the power flow in a transmission line. Because the dynamic process of filter inductance and the switching of converter commonly only affects the high-frequency characteristics larger than kHz [47], whereas the power coupling mainly affects the low-frequency dynamic performance lower than a hundred Hz [34], and the high-frequency disturbance can be handled by the inner loop controller [39], the dynamic process of the power flow can be neglected. After that, there exist $G_{\mathrm{P}\delta}(s)=K_{\mathrm{P}\delta}$, $G_{\mathrm{PE}}(s)=K_{\mathrm{PE}}$, $G_{\mathrm{Q}\delta}(s)=K_{\mathrm{Q}\delta}$, and $G_{\mathrm{QE}}(s)=K_{\mathrm{QE}}$.

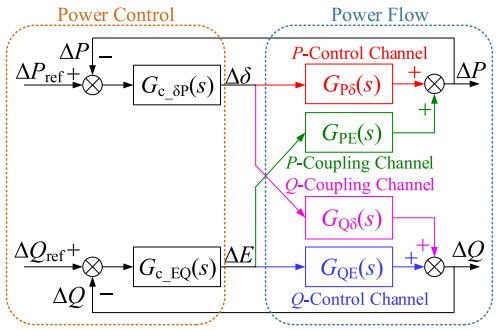


Fig. 3. Unified dynamic power coupling model of a grid-forming converter.

TABLE I
SUMMARY OF MAIN GRID-FORMING CONTROL STRATEGIES

| Active power control | $G_{\mathrm{c\_}\delta\mathrm{P}}(s)$ | Reactive power control | $G_{\mathrm{c\_EQ}}(s)$ |
|---|---|---|---|
| *P*-$\omega$ droop [11] | $\frac{1}{k_{\mathrm{P}}s}$ | *Q*-*V* droop [11] | $\frac{1}{k_{\mathrm{Q}}}$ |
| *P*-$\delta$ droop [15] | $\frac{1}{k_{\mathrm{P}}}$ | *Q*-$\dot{V}$ droop [16] | $\frac{1}{k_{\mathrm{Q}}s}$ |
| Improved *P*-$\omega$ droop #1 [17] | $\frac{1}{k_{\mathrm{P}}s}+\frac{1}{k_{\mathrm{Pd1}}}+k_{\mathrm{Pd2}}s$ | Improved *Q*-*V* droop [17]-[19] | $\frac{1}{k_{\mathrm{Q}}}+k_{\mathrm{Qd}}s$ |
| Improved *P*-$\omega$ droop #2 [18],[19] | $\frac{1}{k_{\mathrm{P}}s}+\frac{1}{k_{\mathrm{Pd}}}$ | Improved *Q*-$\dot{V}$ droop [20] | $\frac{1}{k_{\mathrm{Q}}s}+k_{\mathrm{Qd}}s$ |
| Typical VSG [13] | $\frac{1}{(J\omega_{\mathrm{ref}}s+k_{\mathrm{P}})s}$ | PI control [34] | $k_{\mathrm{p}}+\frac{k_{\mathrm{i}}}{s}$ |
| Droop with lead-lag unit [22] | $\frac{1+T_{\mathrm{a}}s}{k_{\mathrm{P}}s(1+T_{\mathrm{b}}s)}$ | Inertia control [37],[49] | $\frac{1}{J_{\mathrm{Q}}s+k_{\mathrm{Q}}}$ |
| VISMA [21] | $\frac{1}{[J\omega_{\mathrm{ref}}+f(s)k_{\mathrm{P}}]s^2}$ | … | … |
| Phase-feedforward VSG [23] | $\frac{k_{\mathrm{f}}s+1}{(J\omega_{\mathrm{ref}}s+k_{\mathrm{P}})s}$ | \ | \ |
| Generalized droop control [24] | $G_{\mathrm{c\_}\delta\mathrm{P}}(s)=K\frac{(1+\tau_1s)(1+\tau_2s)\cdots(1+\tau_ms)}{s^{v+1}(1+T_1s)(1+T_2s)\cdots(1+T_{n-v}s)}$ | | |
| … | … | \ | \ |

Table I summarizes briefly the main grid-forming control strategies, where the equivalent open loop transfer functions of diverse kinds of active power controllers and reactive power controllers are given. The practical grid-forming schemes can be the pairwise combinations of any active power controllers and reactive power controllers therein.

The unified form of FAA of a grid-forming converter shown in Fig. 3 can be derived as, (14) shown at the bottom of the page where $G_{\rm PF} = G_{{\rm P}\delta}(s)\cdot G_{{\rm c\_}\delta{\rm P}}(s)$, $G_{\rm QF} = G_{\rm QE}(s)\cdot G_{\rm c\_EQ}(s)$, $G_{\rm PC} = G_{\rm PE}(s)\cdot\ G_{\rm c\_EQ}(s)$, $G_{\rm QC} = G_{{\rm Q}\delta}(s)\cdot G_{{\rm c\_}\delta{\rm P}}(s)$. $p_{11}(s)$ and $p_{22}(s)$ represent the closed-loop response characteristics of active power control loop (called *P*-control for short in this article, similarly hereinafter) and reactive power control loop (*Q*-control), respectively. Compared to the traditional closed-loop models assuming the system is decoupled, $p_{11}(s)$ and $p_{22}(s)$ take the effects of power coupling factors into account, and therefore, are more accurate. $p_{11}(s)$ and $p_{22}(s)$ can also be used to the design and stability analysis of active and reactive power controllers, respectively, similar to the traditional closed-loop model [34]. $p_{12}(s)$ reflects the active power response characteristics under reactive power reference disturbance (*P*-coupling). $p_{21}(s)$ reflects the reactive power response under active power reference disturbance (*Q*-coupling). $p_{12}(s)$ and $p_{21}(s)$ characterize directly the closed loop features of the cross-coupling channels.

As it can be seen, the FAA is a function of $s$ instead of being a constant, where $p_{ij}(s)$ represents dynamic FAA of the corresponding channel. Let $s = {\rm j}\omega$, and the FAA will become a matrix in the complex frequency domain, in which the coupling characteristics can be analyzed by the magnitude and phase of each element in FAA. The magnitude of FAA indicates the amplification coefficient under a certain frequency; whereas the phase, which is equivalent to time delay, does not affect the level of coupling, but reflects the travel time of coupling effect from one control channel to another.

In order to assess quantitatively, the power coupling level of grid-forming converters in both dynamic and steady-state operation, this article expands the RGA tool from scalar domain to frequency domain. First, letting $s = {\rm j}\omega$ in $\mathbf{P}(s)$, obtain the FAA $\mathbf{P}({\rm j}\omega)$ in complex frequency domain. Then, calculate the magnitude of each element in $\mathbf{P}({\rm j}\omega)$ to obtain the first amplification magnitude array $\mathbf{P}(\omega)$, which is a function of the frequency. It should be stressed here that in order to represent the directions of gains of the channels, introduce "+" and "−" to distinguish, where "+" represents positive-direction gain, namely increasing the input disturbance causes the output also increase, and "–" represents negative-direction gain, namely increasing the input disturbance will make the output decrease.

For the grid-forming converter system studied in this article, the *Q*-coupling channel (represented by $p_{21}$) is negative-direction gain, whereas others are positive-direction gains. Hence, add "–" before $p_{21}(\omega)$ to get the modified array $\mathbf{P}(\omega)$, and then according to (11) transform $\mathbf{P}(\omega)$ to obtain the unified form of RGA $\mathbf{\Lambda}(\omega)$ in frequency domain. The abovementioned transformation process can be described by

$$\mathbf{P}(s)\xrightarrow{p_{ij}({\rm j}\omega) = p_{ij}(s)}\mathbf{P}({\rm j}\omega)\xrightarrow{p_{ij}(\omega) = |p_{ij}({\rm j}\omega)|}\mathbf{P}(\omega)\xrightarrow[\mathbf{P}\otimes(\mathbf{P}^{-1})^{\rm T}]{-1 * p_{21}(\omega)}\mathbf{\Lambda}(\omega). \tag{15}$$

The final unified form of RGA in frequency domain yields

$$\begin{aligned}\mathbf{\Lambda}(\omega) &= \begin{bmatrix}\lambda_{11}(\omega) & \lambda_{12}(\omega)\\ \lambda_{21}(\omega) & \lambda_{22}(\omega)\end{bmatrix}\\ &= \frac{\begin{bmatrix}p_{11}(\omega)p_{22}(\omega) & -p_{12}(\omega)p_{21}(\omega)\\ -p_{12}(\omega)p_{21}(\omega) & p_{11}(\omega)p_{22}(\omega)\end{bmatrix}}{p_{11}(\omega)p_{22}(\omega) - p_{12}(\omega)p_{21}(\omega)}.\end{aligned} \tag{16}$$

It can be seen from (16) that $\mathbf{\Lambda}(\omega)$ is a function of the frequency, where $\lambda_{ij}(\omega)$ represents the relative gains of input signals of different frequencies. $\mathbf{\Lambda}(\omega)$ satisfies the characteristics of RGA as summarized hereinbefore.

As explained previously, FAA has clearer physical meaning focusing on a special control system, which is advantageous to the straightforward understanding of the coupling relationship between input variables and output variables; while RGA provides a universal dynamic power coupling quantitative analysis tool, which is favorable to the evaluation and comparative analysis of various types of grid-forming schemes. Table II presents the detailed comparison between FAA and RGA models. Due to their respective advantages, the dynamic matrix $\mathbf{P}(s)$ and $\mathbf{\Lambda}(\omega)$ expressed by (14) and (16) based on the generic structure of grid-forming converters depicted in Fig. 3 constitute the whole unified dynamic power coupling model together.

It should be emphasized that the FAA and RGA models can be adapted to all types of grid-forming control schemes by way of substituting the corresponding equivalent open-loop transfer functions into $G_{{\rm c\_}\delta{\rm P}}(s)$ and $G_{\rm c\_EQ}(s)$. However, for lack of space, this article only takes the typical VSG and droop control described by (5)–(7), as examples to explain the application of the proposed model.

## IV. Analysis of Power Coupling Characteristics for VSG and Droop Control

### A. FAA and RGA Model

In regard to VSG control, the transfer functions of active power and reactive power controllers are given by

$$G^{\rm V}_{{\rm c\_}\delta{\rm P}}(s) = 1/[s\,(J\omega_{\rm ref}s + k_{\rm P})],\quad G^{\rm V}_{\rm c\_EQ}(s) = 1/k_{\rm Q}. \tag{17}$$

Typical droop control can be considered as a special VSG with zero virtual inertia. Accordingly, the droop model can be derived from the VSG model by only letting $J = 0$ in (17). For ease of differentiation, when $J = 0$, the superscript "V" can be replaced with "D" in the later section to stress that the corresponding variables are specially used for droop control. Namely, the value of $x^{\rm D}$ equals to that of $x^{\rm V}|_{J\,=\,0}$, where $x$ refers to any variable or function name.

$$\mathbf{P}(s) = \begin{bmatrix}p_{11}(s) & p_{12}(s)\\ p_{21}(s) & p_{22}(s)\end{bmatrix} = \frac{\begin{bmatrix}G_{\rm PF} + G_{\rm PF}G_{\rm QF} - G_{\rm PC}G_{\rm QC} & G_{\rm PC}\\ G_{\rm QC} & G_{\rm QF} + G_{\rm PF}G_{\rm QF} - G_{\rm PC}G_{\rm QC}\end{bmatrix}}{1 + G_{\rm PF} + G_{\rm QF} + G_{\rm PF}G_{\rm QF} - G_{\rm PC}G_{\rm QC}} \tag{14}$$

TABLE II
COMPARISON OF FAA MODEL AND RGA MODEL

| Model type | FAA model | RGA model |
|---|---|---|
| Advantages | -- Straightforward and readily comprehensible description of the relationships between input variables and output variables.<br>-- Clear physical meaning.<br>-- Can observe the unilateral coupling. | -- Universal quantitative analysis index for power coupling level regardless of the particular structures and parameters.<br>-- Easy to evaluate the power coupling level quantitatively.<br>-- Favorable to comparative analysis of various types of grid-forming converters. |
| Disadvantages | -- Not independent against units.<br>-- Cannot analyze and evaluate the coupling quantitatively.<br>-- Not suitable for comparing different grid-forming converters. | -- Cannot observe the unilateral coupling.<br>-- Complicated derivation process. |
| Examples of applicable scenarios | -- Dynamic performance or stability analysis of one particular loop.<br>-- Dynamic response indices for controller design. | -- Quantitative analysis of the power coupling level.<br>-- Comparative analysis among different grid-forming schemes.<br>-- Criterion of power coupling degree for controller design. |

Substituting (17) into (14), the FAA for VSG can be derived as

$$\mathbf{P}^{\mathrm{V}}(s)=\begin{bmatrix} p_{11}^{\mathrm{V}}(s) & p_{12}^{\mathrm{V}}(s) \\ p_{21}^{\mathrm{V}}(s) & p_{22}^{\mathrm{V}}(s) \end{bmatrix} = \begin{bmatrix} \frac{\mu_{11\_0}^{\mathrm{V}}}{\beta_2^{\mathrm{V}}s^2+\beta_1^{\mathrm{V}}s+\beta_0^{\mathrm{V}}} & \frac{\mu_{12\_2}^{\mathrm{V}}s^2+\mu_{12\_1}^{\mathrm{V}}s}{\beta_2^{\mathrm{V}}s^2+\beta_1^{\mathrm{V}}s+\beta_0^{\mathrm{V}}} \\ \frac{\mu_{21\_0}^{\mathrm{V}}}{\beta_2^{\mathrm{V}}s^2+\beta_1^{\mathrm{V}}s+\beta_0^{\mathrm{V}}} & \frac{\mu_{22\_2}^{\mathrm{V}}s^2+\mu_{22\_1}^{\mathrm{V}}s+\mu_{22\_0}^{\mathrm{V}}}{\beta_2^{\mathrm{V}}s^2+\beta_1^{\mathrm{V}}s+\beta_0^{\mathrm{V}}} \end{bmatrix} \tag{18}$$

where

$$\beta_2^{\mathrm{V}}=J\omega_{\mathrm{ref}}+3J\omega_{\mathrm{ref}}I_{\mathrm{c}}\cos\gamma_{\mathrm{c}}/k_{\mathrm{Q}},\ \beta_1^{\mathrm{V}}=k_{\mathrm{P}}+3k_{\mathrm{P}}I_{\mathrm{c}}\cos\gamma_{\mathrm{c}}/k_{\mathrm{Q}}$$
$$\beta_0^{\mathrm{V}}=3E_0I_{\mathrm{c}}\cos\gamma_{\mathrm{c}}+9E_0I_{\mathrm{c}}^2/k_{\mathrm{Q}},\ \mu_{12\_2}^{\mathrm{V}}=3J\omega_{\mathrm{ref}}I_{\mathrm{c}}\sin\gamma_{\mathrm{c}}/k_{\mathrm{Q}}$$
$$\mu_{12\_1}^{\mathrm{V}}=3k_{\mathrm{P}}I_{\mathrm{c}}\sin\gamma_{\mathrm{c}}/k_{\mathrm{Q}},\ \mu_{11\_0}^{\mathrm{V}}=3E_0I_{\mathrm{c}}\cos\gamma_{\mathrm{c}}+9E_0I_{\mathrm{c}}^2/k_{\mathrm{Q}}$$
$$\mu_{21\_0}^{\mathrm{V}}=-3E_0I_{\mathrm{c}}\sin\gamma_{\mathrm{c}},\ \mu_{22\_2}^{\mathrm{V}}=3J\omega_{\mathrm{ref}}I_{\mathrm{c}}\cos\gamma_{\mathrm{c}}/k_{\mathrm{Q}}$$
$$\mu_{22\_1}^{\mathrm{V}}=3k_{\mathrm{P}}I_{\mathrm{c}}\cos\gamma_{\mathrm{c}}/k_{\mathrm{Q}},\ \mu_{22\_0}^{\mathrm{V}}=9E_0I_{\mathrm{c}}^2/k_{\mathrm{Q}}.$$

Then, following the calculation procedure expressed in (15), RGA for VSG can be obtained as:

$$\mathbf{\Lambda}^{\mathrm{V}}(\omega)=\begin{bmatrix} \lambda_{11}^{\mathrm{V}}(\omega) & \lambda_{12}^{\mathrm{V}}(\omega) \\ \lambda_{21}^{\mathrm{V}}(\omega) & \lambda_{22}^{\mathrm{V}}(\omega) \end{bmatrix} = \begin{bmatrix} \lambda_{11}^{\mathrm{V}}(\omega) & 1-\lambda_{11}^{\mathrm{V}}(\omega) \\ 1-\lambda_{11}^{\mathrm{V}}(\omega) & \lambda_{11}^{\mathrm{V}}(\omega) \end{bmatrix} \tag{19}$$

where

$$\lambda_{11}^{\mathrm{V}}(\omega)=\frac{\mu_{11\_0}^{\mathrm{V}}\sqrt{\left(-\mu_{22\_2}^{\mathrm{V}}\omega^2+\mu_{22\_0}^{\mathrm{V}}\right)^2+\mu_{22\_1}^{\mathrm{V2}}\omega^2}}{\begin{bmatrix} \mu_{11\_0}^{\mathrm{V}}\sqrt{\left(-\mu_{22\_2}^{\mathrm{V}}\omega^2+\mu_{22\_0}^{\mathrm{V}}\right)^2+\mu_{22\_1}^{\mathrm{V2}}\omega^2} \\ -\mu_{21\_0}^{\mathrm{V}}\sqrt{\mu_{12\_1}^{\mathrm{V2}}\omega^2+\mu_{12\_2}^{\mathrm{V2}}\omega^4} \end{bmatrix}}. \tag{20}$$

It is worth mentioning that the superscript "2" of each variable means square, similarly hereafter.

The limits of the FAA and RGA for VSG at $s=0$ and $s=\infty$ yield

$$\lim_{s\to 0}\mathbf{P}^{\mathrm{V}}=\begin{bmatrix} p_{11}^{\mathrm{V},s\to 0} & p_{12}^{\mathrm{V},s\to 0} \\ p_{21}^{\mathrm{V},s\to 0} & p_{22}^{\mathrm{V},s\to 0} \end{bmatrix} = \begin{bmatrix} 1 & 0 \\ \frac{-\sin\gamma_{\mathrm{c}}}{\cos\gamma_{\mathrm{c}}+I_{\mathrm{c}}/k_{\mathrm{Q}}} & \frac{I_{\mathrm{c}}}{k_{\mathrm{Q}}\cos\gamma_{\mathrm{c}}+I_{\mathrm{c}}} \end{bmatrix} \tag{21}$$

TABLE III
MAIN PARAMETERS OF GRID-FORMING CONVERTER

| Parameters | Values | Parameters | Values |
|---|---|---|---|
| $S_{\mathrm{b}}$ | 10 kVA | $J$ | 1 kg·m$^2$ |
| $U_{\mathrm{b}}$ | 380 V | $k_{\mathrm{P}}$ | 10000 W/Hz |
| $R$ | 0.1 p.u. | $k_{\mathrm{Q}}$ | 1000 Var/V |
| $X$ | 0.3 p.u. | $\omega_{\mathrm{ref}}$ | 100π rad/s |
| $f_{\mathrm{s}}$ | 10 kHz | $E_{\mathrm{ref}}$ | 311 V |
| $P_{\mathrm{ref}}$ | 5000 W | $Q_{\mathrm{ref}}$ | 5000 Var |

$$\lim_{s\to\infty}\mathbf{P}^{\mathrm{V}}=\begin{bmatrix} p_{11}^{\mathrm{V},s\to\infty} & p_{12}^{\mathrm{V},s\to\infty} \\ p_{21}^{\mathrm{V},s\to\infty} & p_{22}^{\mathrm{V},s\to\infty} \end{bmatrix} = \begin{bmatrix} 0 & \frac{I_{\mathrm{c}}\sin\gamma_{\mathrm{c}}/k_{\mathrm{Q}}}{1+I_{\mathrm{c}}\cos\gamma_{\mathrm{c}}/k_{\mathrm{Q}}} \\ 0 & \frac{I_{\mathrm{c}}\cos\gamma_{\mathrm{c}}/k_{\mathrm{Q}}}{1+I_{\mathrm{c}}\cos\gamma_{\mathrm{c}}/k_{\mathrm{Q}}} \end{bmatrix} \tag{22}$$

$$\lim_{\omega\to 0}\mathbf{\Lambda}^{\mathrm{V}}=\begin{bmatrix} \lambda_{11}^{\mathrm{V},\omega\to 0} & \lambda_{12}^{\mathrm{V},\omega\to 0} \\ \lambda_{21}^{\mathrm{V},\omega\to 0} & \lambda_{22}^{\mathrm{V},\omega\to 0} \end{bmatrix} = \begin{bmatrix} 1 & 0 \\ 0 & 1 \end{bmatrix} \tag{23}$$

$$\lim_{\omega\to\infty}\mathbf{\Lambda}^{\mathrm{V}}=\begin{bmatrix} \lambda_{11}^{\mathrm{V},\omega\to\infty} & \lambda_{12}^{\mathrm{V},\omega\to\infty} \\ \lambda_{21}^{\mathrm{V},\omega\to\infty} & \lambda_{22}^{\mathrm{V},\omega\to\infty} \end{bmatrix} = \begin{bmatrix} \frac{\cos\gamma_{\mathrm{c}}{}^2+3I_{\mathrm{c}}\cos\gamma_{\mathrm{c}}/k_{\mathrm{Q}}}{1+3I_{\mathrm{c}}\cos\gamma_{\mathrm{c}}/k_{\mathrm{Q}}} & \frac{\sin\gamma_{\mathrm{c}}{}^2}{1+3I_{\mathrm{c}}\cos\gamma_{\mathrm{c}}/k_{\mathrm{Q}}} \\ \frac{\sin\gamma_{\mathrm{c}}{}^2}{1+3I_{\mathrm{c}}\cos\gamma_{\mathrm{c}}/k_{\mathrm{Q}}} & \frac{\cos\gamma_{\mathrm{c}}{}^2+3I_{\mathrm{c}}\cos\gamma_{\mathrm{c}}/k_{\mathrm{Q}}}{1+3I_{\mathrm{c}}\cos\gamma_{\mathrm{c}}/k_{\mathrm{Q}}} \end{bmatrix}. \tag{24}$$

### B. FAA Analysis

The main parameters of grid-forming converter used for analysis in this section are shown in Table III, where $f_{\mathrm{s}}$ is the switching frequency of converter, $S_{\mathrm{b}}$ and $U_{\mathrm{b}}$ are the base values of power and voltage, respectively, which are equal to the nominal power and nominal phase-to-phase voltage of the converter. In the later analysis, except for the changing parameter, the other parameters were chosen according to Table III.

First, the bode diagrams of FAA with different $J$, $k_{\mathrm{P}}$, and $k_{\mathrm{Q}}$ are shown in Figs. 4–6, respectively. It should be noted that the unit of magnitude in the bode diagram is absolute value instead of being logarithm in order to facilitate observing and assessing the coupling level.

*1) Droop Control ($J=0$):*

*a) P-Coupling Analysis:* For droop control, namely $J=0$, it can be observed from the bode diagrams that $p_{11}^{D}(s)$ exhibits

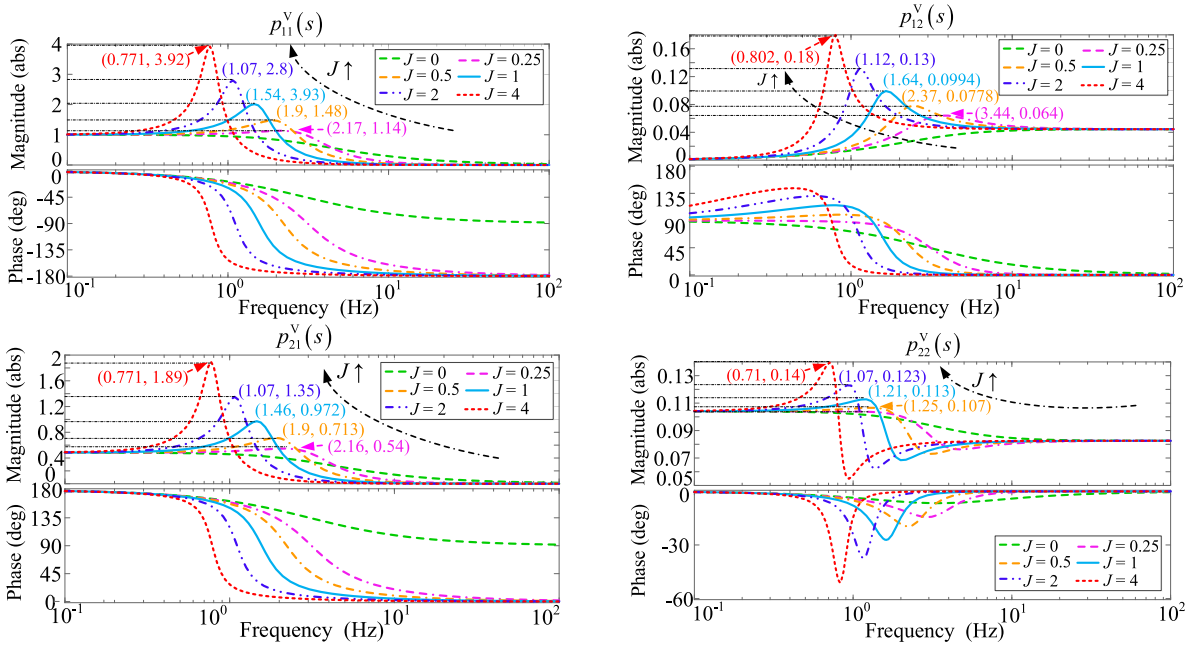


Fig. 4. Bode diagrams of FAA with different values of $J$ ($J$ varies from 0 to 4 kg·m$^2$).

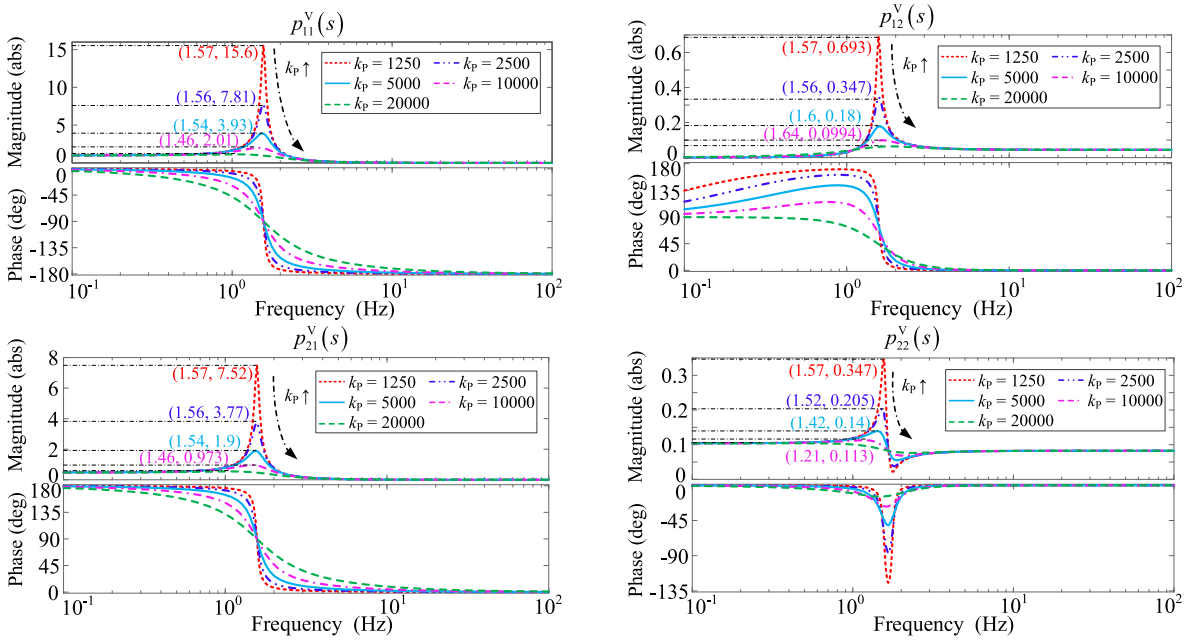


Fig. 5. Bode diagrams of FAA with different values of $k_P$ ($k_P$ varies from 1250 W/Hz to 20 000 W/Hz).

a low-pass characteristic while $p_{12}^{D}(s)$ has a high-pass characteristic, and the cutoff frequency $f_c$ is around the bandwidth of grid-forming controller, depending on the control parameters inside. In the frequency region larger than $f_c$, $p_{11}^{D}(s)$ tends to be zero, indicating that $P$-control loop possesses the capability of suppressing high frequency perturbation. While $p_{12}^{D}(s)$ is always larger than zero and finally approaches its limit value at $s = \infty$ ($p_{12}^{D,s\to\infty} > 0$), which reveals that there exists $P$-coupling for high frequency signal. Hence, the high frequency perturbation occurred in the $Q$-control loop, e.g., the high-frequency component involved in a step input, will transmit to the $P$-control loop and may cause a transient response in the active power. Conversely, in the frequency region smaller than $f_c$, $p_{11}^{D}(s)$ moves towards its limit value 1 at $s = 0$ and $p_{12}^{D}(s)$ tends to be 0. It means that the steady-state value of output active power is not affected by the coupling anymore and it can track the active

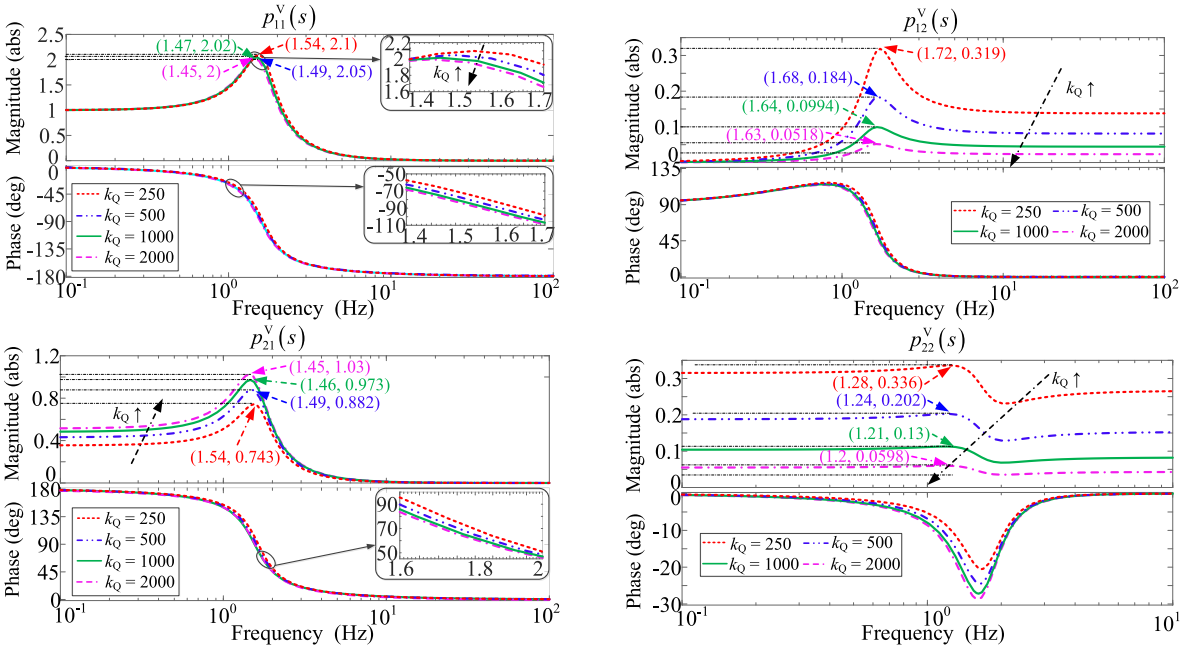


Fig. 6. Bode diagrams of FAA with different values of $k_Q$ ($k_Q$ varies from 250 Var/V to 2000 Var/V).

power reference accurately. This is because the integral in the active power controller eliminates the error eventually.

*b) Q-Coupling Analysis:* Similarly, the reactive power response characteristics are depicted by $p_{21}^{D}(s)$ and $p_{22}^{D}(s)$. It can be seen from the bode diagrams, both $p_{21}^{D}(s)$ and $p_{22}^{D}(s)$ exhibit low-pass characteristics with $f_c$ as cut frequency. It means that the *Q*-coupling frequency band is located at the low frequency region, which is opposite to the *P*-coupling. The overlap of the passband of *P*-control channel and *Q*-coupling channel means that the low-frequency component coupled from *P*-control loop will not be filtered adequately by the reactive power controller.

The steady-state value $p_{21}^{\mathrm{D},s\to 0}$, mathematically expressed in (21), is not equal to zero, which implies that the steady-state value of the output reactive power is affected by the *Q*-coupling and will produce a visible error if a variation occurs in the active power steady-state operating point. Besides, it can be concluded from (21) that the error is mainly related to the impedance ratio, the modulus of impedance, power angle, voltage, and reactive power droop coefficient. Besides, $\angle p_{21}^{D,s\to\infty} = 180^\circ$ indicates the negative correlation between the active power reference disturbance and the corresponding reactive power output. In the other words, an increase of active power reference will cause a drop in reactive power. On the contrary, since $p_{21}^{D,s\to\infty} = 0$, the high frequency disturbance of active power has little coupling effect on the reactive power control channel.

With the increase of frequency, $p_{22}^{D}(s)$ goes down to a constant, which is greater than zero, and does not change with $k_P$. It means that the reactive power loop can attenuate the high frequency disturbance as well, but the rejection ability is weaker than active power loop.

*2) VSG Control ($J > 0$):* It can be seen from (21)–(24) that $J$ is irrelevant to the limits, indicating that the limits of $\mathbf{P}^{V}$ and $\mathbf{\Lambda}^{V}$ with regard to VSG control at $s = 0$ and $s = \infty$ are equal to those of $\mathbf{P}^{D}$ and $\mathbf{\Lambda}^{D}$ with regard to droop control. Hence, VSG has the same steady-state power coupling characteristics with droop control. However, different from droop control, VSG control introduces a resonance peak, which will amplify the coupling effect between the power loops. As it can be seen from the bode plots, the resonance peak is probably several times as high as the steady-state gain. Therefore, the power coupling of VSG system is much more serious than in the droop-controlled system. Furthermore, the resonance frequency is located at the natural frequency of the VSG active power control loop. As a consequence, the probable active power oscillation will become the excitation source of the coupling resonance. The dynamic responses of the active power and reactive power will both exhibit oscillations before reaching steady state.

There are three key parameters in VSG control, namely the virtual inertia $J$, active power droop coefficient (damping factor) $k_P$, and reactive power droop coefficient $k_Q$, which play important roles in power coupling characteristics.

*a) The Effect of J.:* Because the limits at steady state ($s = 0$) of FAAs and RGAs of VSG are the same with those of droop-controlled converter, the virtual inertia $J$ introduced by VSG control, has no impact on the static coupling. But the virtual inertia $J$ has a significant impact on the resonance features of FAA and RGA (RGA will be analyzed in the following section), which indicates the dynamic coupling characteristics of grid-forming converter. From the bode diagrams of $p_{12}^{V}(s)$ and $p_{21}^{V}(s)$ shown in Fig. 4, it can be seen that when $J$ increases, the resonance peak will become larger and the resonance frequency will decrease. It means that more oscillatory active power and reactive power response waveforms with smaller fluctuating frequency and longer settling time will occur caused by a step input of power reference.

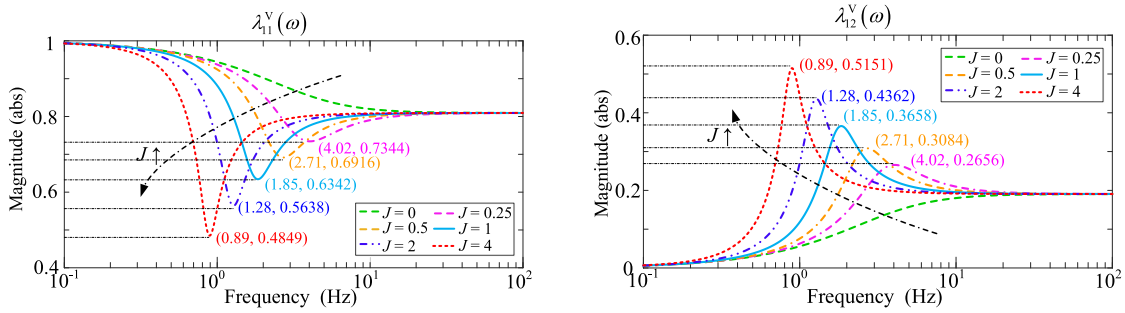


Fig. 7. Bode diagrams of $\lambda_{11}^{V}(\omega)$ and $\lambda_{12}^{V}(\omega)$ with different values of $J$ ($J$ varies from 0 to 4 kg·m$^2$).

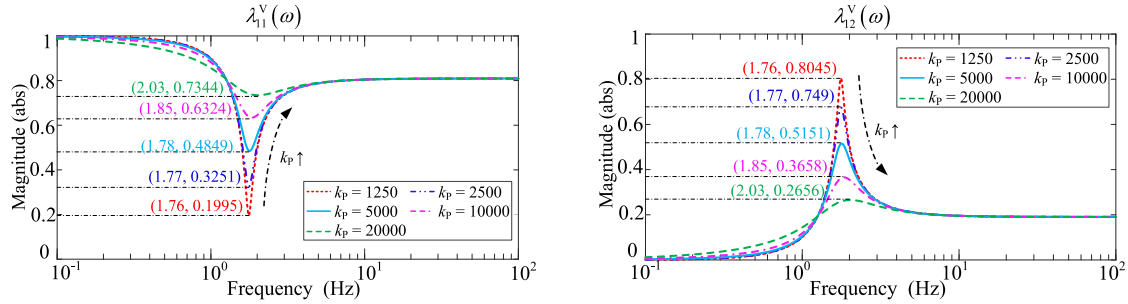


Fig. 8. Bode diagrams of $\lambda_{11}^{V}(\omega)$ and $\lambda_{12}^{V}(\omega)$ with different values of $k_P$ ($k_P$ varies from 1250 W/Hz to 20 000 W/Hz).

*b) The Effect of $k_P$.:* According to (21), the limit of $\mathbf{P}^{V}$ is irrelevant to $k_P$, so $k_P$ does not affect the steady-state coupling. Besides the droop effect, another important effect of $k_P$ is to increase the damping ratio of active power loop and suppress oscillation. Moreover, it is shown in Fig. 5 that $k_P$ can also suppress the resonance peaks of *P*-coupling, *Q*-coupling and *Q*-control channels. Therefore, adding damping can mitigate the coupling between power loops effectively. However, there is an inherent tradeoff within primary frequency regulation requirement, power oscillation suppression performance, and dynamic response time [48], which restricts the effect of $k_P$ on eliminating oscillation as the consequence of power dynamic coupling. It can also be seen from the Bode diagrams that adding damping scarcely changes the location of resonance frequency and, thus, has little impact on the frequency of system oscillation. Because $k_P$ cannot change the steady-state gain of FAA, adding damping is incapable of eliminating the steady-state error of reactive power caused by the power coupling.

*c) The Effect of $k_Q$.:* According to Fig. 6, increasing $k_Q$ can remarkably reduce the value of $p_{12}^{V}(s)$ in the high frequency region and restrain the resonance peak of $p_{12}^{V}(s)$. Therefore, the increase of $k_Q$ can contribute to mitigating the *P*-coupling. Conversely, enlarging $k_Q$ would amplify $p_{21}^{V}(s)$ and reduce $p_{22}^{V}(s)$, which means the augmentation of $k_Q$ will worsen *Q*-coupling and produce greater error of reactive power. Meanwhile, adding $k_Q$ can also make the resonance frequency decrease slightly due to the rise of time constant of reactive power loop. But the time constant of reactive power loop is much smaller than that of active power loop, so the change in resonance frequency is not quite obvious.

## C. RGA Analysis

Figs. 7–9 show the bode diagrams of RGA with different $J$, $k_P$ and $k_Q$.

Although the RGA is a unit matrix at steady state as expressed mathematically in (23), a special coupling form between the two power control loops still exists. As it can be seen from (21), $p_{12}^{V,s\to 0}$ and $p_{21}^{V,s\to 0} \neq 0$. It indicates the active power reference disturbance has a coupling influence on the output reactive power, but this influence will not go back to affect the active power. Consequently, the coupling can still cause the steady-state error of reactive power and this issue needs to be addressed as well.

In the region where frequency is larger than $f_c$, $\lambda_{11}^{D}(\omega)$ moves away from 1, which shows us a strong coupling in the dynamic process. The same conclusion has also been drawn by the FAA analysis.

According to (23) and (24), the limit of $\lambda_{11}^{V}(\omega)$ at $\omega = 0$ and $\omega = \infty$ can be derived as

$$\lambda_{11}^{V,\omega\to 0} = \lim_{\omega\to 0} \lambda_{11}^{V}(\omega) = 1 > K_{P\delta} \tag{25}$$

$$\begin{aligned}\lambda_{11}^{V,\omega\to\infty} &= \lim_{\omega\to\infty} \lambda_{11}^{V}(\omega) = \frac{\cos^2\gamma_c + 3I_c\cos\gamma_c/k_Q}{1+3I_c\cos\gamma_c/k_Q} \\ &= 1 - \frac{\sin^2\gamma_c}{1+3I_c\cos\gamma_c/k_Q} > 1-\sin^2\gamma_c \\ &= \cos^2\gamma_c = K_{P\delta}.\end{aligned} \tag{26}$$

For droop control, $\lambda_{11}^{V}(\omega)$ is the monotonic function of $\omega$ and obeys the relationship of (25) and (26). Therefore, the relative

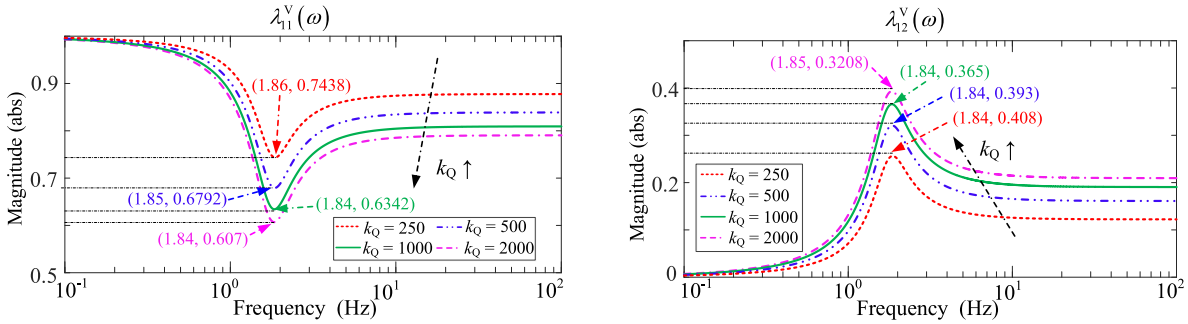


Fig. 9. Bode diagrams of $\lambda_{11}^{V}(\omega)$ and $\lambda_{12}^{V}(\omega)$ with different values of $k_Q$ ($k_Q$ varies from 250 Var/V to 2000 Var/V).

gain of droop-controlled system $\lambda_{11}^{V}(\omega)$ is always larger than that of power flow without control system, which indicates that the closed-loop droop control is helpful in weakening the power coupling.

Different from the droop control, although the limits of relative gains $\lambda_{11}^{V,\omega\to 0}$ and $\lambda_{11}^{V,\omega\to\infty}$ are smaller than the relative gains in power flow, the relative gain $\lambda_{12}^{V}(\omega)$ of VSG becomes much larger than 1 in the vicinity of the resonance frequency due to the appearance of resonance peak, which represents a strong coupling. Consequently, the VSG control is prone to amplify the coupling in further and produce an oscillation in both active power and reactive power. So, compared to droop control, the power coupling of VSG is a more pressing problem needed to be dealt with.

On the whole, according to the bode diagrams of RGA shown in Figs. 7–9, the effects of control parameters on the system coupling characteristics can be concluded as follows.

1) Increasing virtual inertia $J$ will add the coupling level and reduce the coupling frequency.
2) Adding droop coefficient (damping factor) $k_P$ will mitigate the coupling effectively and not change the coupling frequency, but the effect is probably limited due to the tradeoff within primary frequency regulation requirement, power oscillation suppression performance.
3) Enlarging reactive power coefficient $k_Q$ will worsen the power coupling in a moderate degree and lower the coupling frequency slightly.

Except for the dynamic indices calculated by the FAA, according to the RGA theory, the criterion of coupling level determined by the RGA further provides the novel rules for parameter design of droop and VSG controllers by setting proper value of $\lambda_{11}^{V}$.

## V. Experimental Results

The experiments were conducted by using a hardware-in-the-loop (HIL) platform to verify the correctness of the theoretical analysis.

The setup and photograph of the HIL platform are shown in Fig. 10 . First, the plant model, which is initially built, compiled and downloaded via the host machine before the test, operates in real time with a step size of 8 $\mu$s in the target machine. Then, the control algorithm of the grid-forming converters runs in a

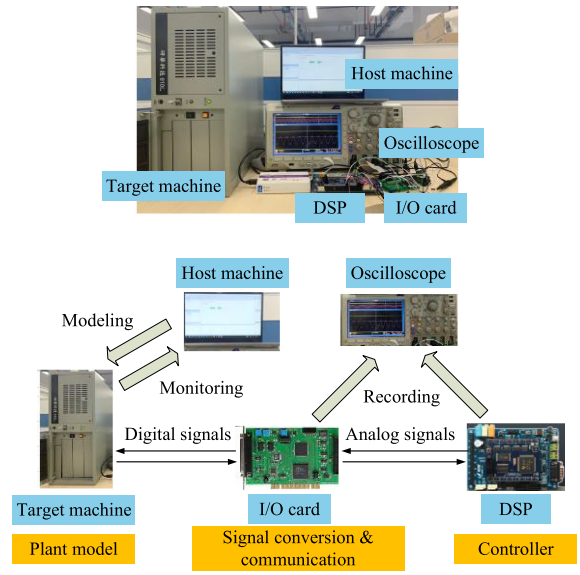


Fig. 10. Photograph and setup of the HIL platform.

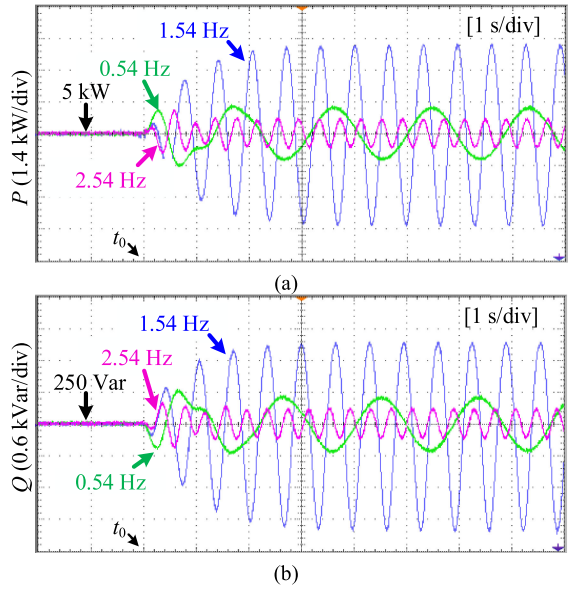


Fig. 11. $Q$-dynamic coupling characteristics of VSG in the vicinity of resonance frequency. (a) Active power. (b) Reactive power.

TABLE IV
*Q*-DYNAMIC COUPLING GAIN INDICES UNDER $P_{REF}$ DISTURBANCE

| Frequencies of $P_{ref}$ | | 1.54 Hz | | 2.54 Hz | | 0.54 Hz | |
|---|---|---|---|---|---|---|---|
| Observation items | | *P* | *Q* | *P* | *Q* | *P* | *Q* |
| Gains | Model | 3.94 | 1.90 | 0.61 | 0.30 | 1.13 | 0.54 |
| | Experiment | 3.98 | 1.77 | 0.62 | 0.27 | 1.11 | 0.50 |

DSP TMS320F28335 whose clock cycle is 1/150 $\mu$s. Third, a multifunction I/O card Humusoft MF624 is embedded in the target machine and used for the A/D and D/A conversion, scaling and communication of the signals between the target machine and DSP peripheral circuit. Finally, the waveforms and data from the target machine and the DSP are monitored and recorded by an oscilloscope in real time.

The tested circuit configuration and parameters are the same with those for the foregoing theoretical analysis, as shown in Fig. 2(a) and Table III.

### A. Dynamic Coupling Characteristics of VSG

*1) Q-Dynamic Coupling:* According to the theoretical modeling and analysis, compared to the droop control, a resonance peak exists in VSG, which will amplify the coupling. When $k_P = 5000$, the resonance peak is located at 1.54 Hz. In order to verify the effects of resonance on the power coupling, the ac responses of power were investigated. First, *Q*-dynamic coupling, namely the effects of the active power disturbance on output reactive power, was investigated. Before $t_0$, the system operated in the steady state with $P_{ref} = 5000$ W and $Q_{ref} = 5000$ Var. At $t = t_0$, different disturbances with the same magnitude (1000 W) and different frequencies (1.54 Hz, 2.54 Hz, and 0.54 Hz) were added to the active power reference $P_{ref}$. The ac response waveforms of active power and reactive power are shown in Fig. 11, and the corresponding indices are given in Table IV.

It can be seen that at the location of resonance frequency 1.54 Hz, under the same-sized excitation, both the active power and reactive power are amplified several times (3.98 times and 1.77 times, respectively). On both sides of the resonance frequency, the amplification gains are lowered.

*2) P-Dynamic Coupling:* Compared to the *Q*-dynamic coupling, several special points need to be considered for the *P*-dynamic coupling. Except for the upward resonance peak in $p_{22}^V(s)$, there also exists another downward resonance peak. The inherent frequency brought by the virtual inertia control is located between the two resonance frequencies, which can be explained by the experimental waveforms under sinusoidal disturbances of the reactive power reference of 1.45 Hz, 1.63 Hz, 1.88 Hz, which are corresponding to the upward resonance frequency, inherent frequency, and downward resonance frequency, respectively. Similarly, before $t_0$, the system operated in the steady state with $P_{ref} = 5000$ W and $Q_{ref} = 5000$ Var. At $t = t_0$, the disturbances with the same magnitude (10000 Var) and different frequencies (1.45 Hz, 1.63 Hz, 1.88 Hz) were added to the reactive power reference $Q_{ref}$. The waveforms are shown in Fig. 12 and the corresponding indices are listed in Table V.

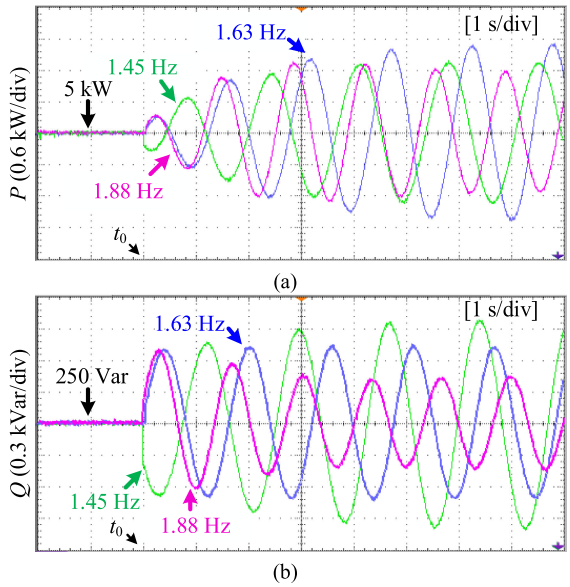


Fig. 12. *P*-dynamic coupling characteristics of VSG in the vicinity of resonance frequency. (a) Active power. (b) Reactive power.

TABLE V
*P*-DYNAMIC COUPLING GAIN INDICES UNDER $Q_{REF}$ DISTURBANCE

| Frequencies of $Q_{ref}$ | | 1.45 Hz | | 1.63 Hz | | 1.88 Hz | |
|---|---|---|---|---|---|---|---|
| Observation items | | *P* | *Q* | *P* | *Q* | *P* | *Q* |
| Gains | Model | 0.12 | 0.13 | 0.17 | 0.099 | 0.12 | 0.060 |
| | Experiment | 0.13 | 0.13 | 0.17 | 0.095 | 0.12 | 0.059 |

The active power has maximum response at 1.63 Hz, while the responses at 1.45 Hz and 1.88 Hz are attenuated, which coincides with the bode diagram of $p_{21}^V(s)$ shown in Fig. 6. The response of reactive power has maximum value at 1.45 Hz, while the response at 1.88 Hz is smallest because of the downward resonance peak at 1.88 Hz as shown in the bode diagram of $p_{22}^V(s)$ of Fig. 6. As a consequence, the relative gain of *P*-coupling channel at 1.88 Hz becomes very large and the severest coupling case occurs the vicinity of this frequency, which is in accord with the conclusion drawn by the Bode diagram of RGA plotted in Fig. 9.

### B. Effects of Pivotal Control Parameters on Power Coupling Characteristics

*1) Virtual Inertia J:* Fig. 13 shows the active and reactive power response waveforms of droop control and VSG with a step change in active power reference for different values of *J*. At $t = t_0$, the active power reference steps from 5000 W to 6000 W. Fig. 14 shows the same waveforms under the conditions of reactive power reference step. At $t = t_0$, the reactive power output is stepped from 250 to 970 Var. It should be also noted that the red thin dashed lines in Fig. 13, Fig. 14 and the following figures are the results of theoretical model and they coincide with the experimental results drawn by the colored thick solid lines, which verifies the correctness of the established model.

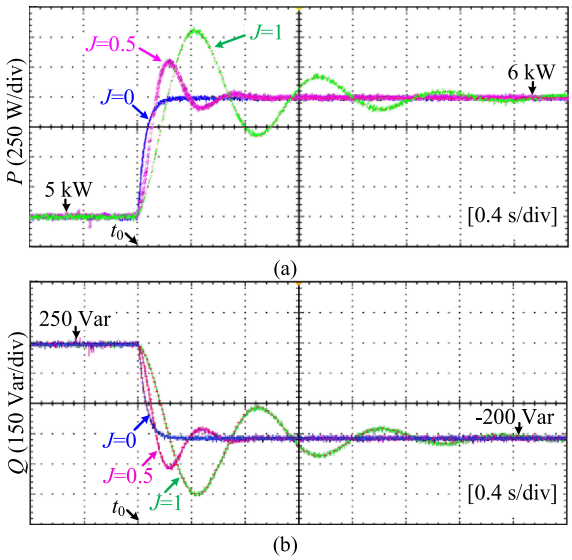


Fig. 13. Power response waveforms of grid-forming converter under active power command step with different *J*. (a) Active power. (b) Reactive power.

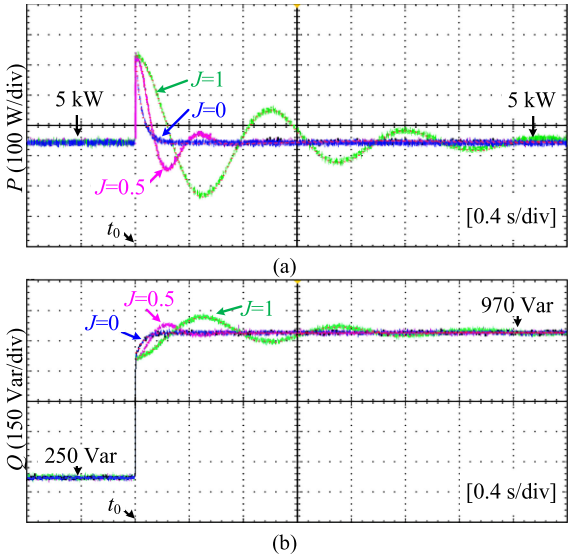


Fig. 14. Power response waveforms of grid-forming converter under reactive power command step with different *J*. (a) Active power. (b) Reactive power.

It can be seen from Fig. 13 that when the output active power changes, the output reactive power also changes unexpectedly, i.e., the change in the active control loop is transmitted to the reactive control loop, which affects the output reactive power. Similarly, Fig. 14 shows that when the output reactive power changes, the output active power also produces unwanted changes, which means the change in the reactive power control loop is transmitted to the active power control loop. The reason is that when the system is originally designed, the assumption that the system is decoupled cannot always be guaranteed, which causes the errors and irrationality.

From the experimental waveforms, it can clearly be seen that under different control strategies or parameters, the coupling level between the two power loops is different. When droop control is used ($J = 0$), since there is no resonance peak, the system can be equivalent to a first-order system, and no overshoot occurs during the dynamic response consequently. However, due to the power coupling, when the active power step is 1000 W, the output reactive power drops from 250 to −200 Var, resulting in a steady-state error of 450 Var. When *J* increases, the system changes from droop control to VSG control mode, the overshoot gradually increases, the oscillation gets larger, the oscillation frequency decreases, and the adjustment time becomes longer. These phenomena validate the potential amplification effects of VSG strategies on the power coupling compared to droop control, which is discovered by the theoretical analysis from the RGA model hereinbefore.

Since the time constant of the reactive power control loop is small, the reactive power response speed is fast and the rise time is very short under the reactive power reference step. However, meanwhile, due to the effect of power coupling, the active power also has an overshoot with very small response time, which in turn causes the adjustment effect of the active power control loop. Particularly, the oscillation process will occur when the virtual inertia becomes large, and the active power oscillation process will be coupled to the reactive power control loop, so that the oscillation process with the same power time constant is also generated in the reactive power loop, which seriously affects the control performance of reactive power. Similarly, the oscillating change of reactive power is coupled into the active power control loop again. Such vicious cycle makes the power response of the VSG system become worse.

From the experimental waveforms, it can be seen that under both working conditions, the steady-state values of active power and reactive power are constant for different *J*. It means that the virtual inertia has no effect on the static coupling of the system. Hence, it proves the correctness of the aforementioned theoretical analysis.

*2) Active Power Droop Coefficient (Damping Factor) $k_P$:* Fig. 15 shows the active and reactive power response waveforms of droop-controlled converter and VSG under active power command step with different $k_\mathrm{P}$. At $t = t_0$, the active power command is stepped from 5000 to 6000 W. Fig. 16 shows the same waveforms under the conditions of reactive power command step. At $t = t_0$, the reactive power output is stepped from 250 to 970 Var.

In the previous Bode plot analysis, it has been proved that increasing the damping will hardly change the position of the resonance frequency, so the impact on the system oscillation frequency is also small. It can be seen from the experimental waveform that as $k_\mathrm{P}$ increases, the oscillation of active power and reactive power is gradually suppressed, and the adjustment time becomes shorter. It can be also observed that the change of $k_\mathrm{P}$ has no effect on the oscillation frequency. However, there is an inherent tradeoff among the primary frequency modulation requirements, power oscillation suppression performance, and dynamic response time, which limits the damping effectiveness to eliminate oscillation.

Since $k_\mathrm{P}$ fails to change the steady-state gain of FAA according to (21), regulating $k_\mathrm{P}$ does not affect the static coupling

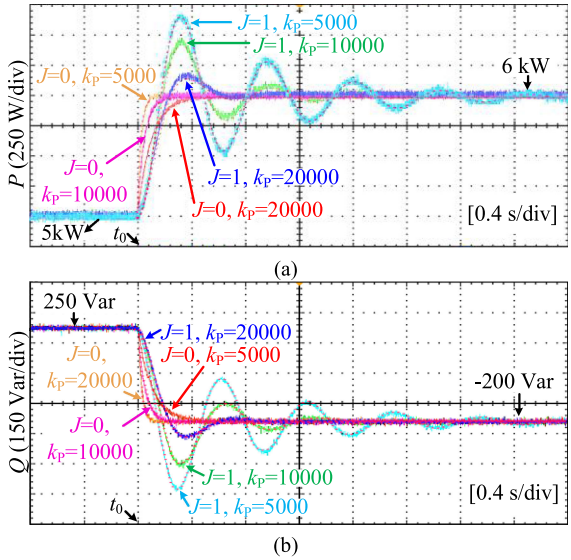


Fig. 15. Power response waveforms of grid-forming converter under active power command step with different $k_{\mathrm{P}}$. (a) Active power. (b) Reactive power.

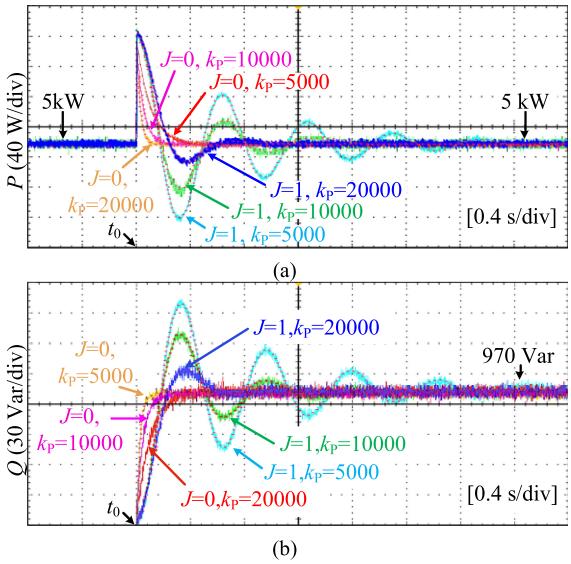


Fig. 16. Power response waveforms of grid-forming converter under reactive power command step with different $k_{\mathrm{P}}$. (a) Active power. (b) Reactive power.

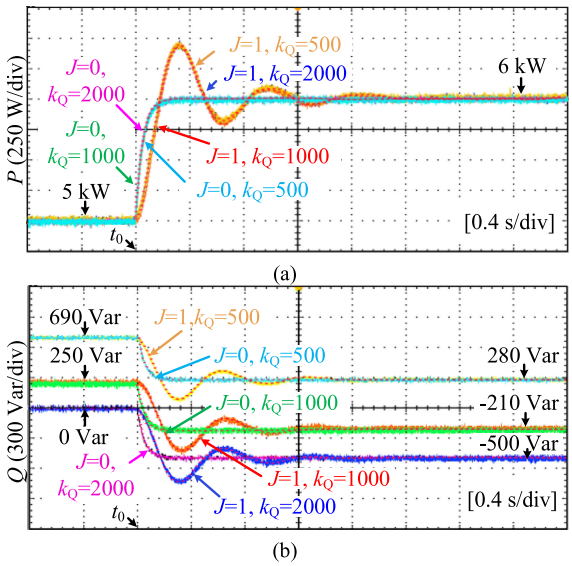


Fig. 17. Power response waveforms of grid-forming converter under active power command step with different $k_{\mathrm{Q}}$. (a) Active power. (b) Reactive power.

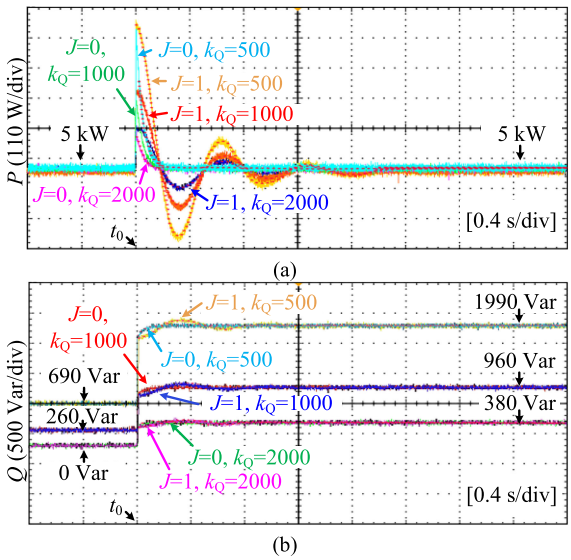


Fig. 18. Power response waveforms of grid-forming converter under reactive power command step with different $k_{\mathrm{Q}}$. (a) Active power. (b) Reactive power.

and thereby is incapable of eliminating the steady-state error of reactive power caused by the power coupling.

*3) Reactive Power Droop Coefficient $k_Q$:* Fig. 17 shows the active power and reactive power response waveforms of grid-forming converter under active power command step with different $k_{\mathrm{Q}}$. At $t = t_0$, the active power command is stepped from 5000 W to 6000 W. Fig. 18 shows the same waveforms under the conditions of the same reactive power command step.

It can be seen from Fig. 17(a), the change of $k_{\mathrm{Q}}$ has little impact on *P*-control channel. In contrast, as shown in Fig. 17(b), with the increase of $k_{\mathrm{Q}}$, the steady-state value of output reactive power declines while the error of output reactive power increases from 410 to 500 Var, which reveals that the augmentation of $k_{\mathrm{Q}}$ will worsen *Q*-coupling.

According to Fig. 18(a), with the increase of $k_{\mathrm{Q}}$, the steady-state value of output active power remains unchanged, while the overshoot decreases, oscillation recedes, settling time gets shorter. It indicates enlarging $k_{\mathrm{Q}}$ is helpful in alleviating *P*-coupling.

As shown in Fig. 18(b), with the increase of $k_{\mathrm{Q}}$, the steady-state value of output reactive power declines while the error of output reactive power increases from 380 to 1300 Var, which reveals that the augmentation of $k_{\mathrm{Q}}$ will enlarge the control error of reactive power. In the meanwhile, compared to the active power, reactive power has shorter settling time, and weaker oscillation.

The abovementioned experimental results coincide closely with the theoretical analysis.

## VI. Conclusion

This article has proposed a unified dynamic power coupling model for grid-forming converter, by building the FAA in the $s$ domain and the extended RGA in the $\omega$ domain of the whole grid-forming converter system. The proposed model provides a universal dynamic power coupling quantitative analysis tool that applies to various types of grid-forming schemes. As an application example, the power coupling characteristics for typical droop control and VSG control has been analyzed in depth by plotting bode diagrams of the proposed model. One of the findings is that, in contrast to the weakening effect of droop control, VSG control has potential risk of amplifying the power coupling. Consequently, not only a visible steady-state error of reactive power, but also long-term oscillations of both active power and reactive power will be raised. Moreover, the effects of the pivotal control parameters are discussed in detail. The rules that have been discovered in this article are helpful to design the parameters of droop and VSG controllers to obtain better power response performance of grid-forming converters. The conclusions drawn by theoretical modeling and analysis were validated by experimental results finally. In the future, the unified dynamic power coupling model will be further used to analyze a system including multiple grid-forming converters.

## References


[1] F. Blaabjerg, Z. Chen, and S. B. Kjaer, "Power electronics as efficient interface in dispersed power generation systems," *IEEE Trans. Power Electron.,* vol. 19, no. 5, pp. 1184–1194, Sep. 2004.

[2] J. M. Carrasco *et al.*, "Power-electronic systems for the grid integration of renewable energy sources: A survey," *IEEE Trans. Ind. Electron.,* vol. 53, no. 4, pp. 1002–1016, Aug. 2006.

[3] F. Blaabjerg, R. Teodorescu, M. Liserre, and A. V. Timbus, "Overview of control and grid synchronization for distributed power generation systems," *IEEE Trans. Ind. Electron.,* vol. 53, no. 5, pp. 1398–1409, Oct. 2006.

[4] J. Rocabert, A. Luna, F. Blaabjerg, and P. Rodriguez, "Control of power converters in AC microgrids," *IEEE Trans. Power Electron.,* vol. 27, no. 11, pp. 4734–4749, Nov. 2012.

[5] X. Fu *et al.*, "Large-signal stability of grid-forming and grid-following controls in voltage source converter: A comparative study," *IEEE Trans. Power Electron.,* vol. 36, no. 7, pp. 7832–7840, Jul. 2021.

[6] W. Du *et al.*, "Modeling of grid-forming and grid-following inverters for dynamic simulation of large-scale distribution systems," *IEEE Trans. Power Del.*, vol. 36, no. 4, pp. 2035–2045, Aug. 2021.

[7] B. Kroposki *et al.*, "Achieving a 100% renewable grid: Operating electric power systems with extremely high levels of variable renewable energy," *IEEE Power Energy Mag,* vol. 15, no. 2, pp. 61–73, Apr. 2017.

[8] D. Pattabiraman, R. H. Lasseter, and T. M. Jahns, "Comparison of grid following and grid forming control for a high inverter penetration power system," in *Proc. IEEE PES Gen. Meeting*, Portland, OR, USA, 2018, pp. 1–5.

[9] R. H. Lasseter, Z. Chen, and D. Pattabiraman, "Grid-forming inverters: A critical asset for the power grid," *IEEE J. Emerg. Sel. Topics Power Electron.,* vol. 8, no. 2, pp. 925–935, Jun. 2020.

[10] Q. C. Zhong, "Power-electronics-enabled autonomous power systems: Architecture and technical routes," *IEEE Trans. Ind. Electron.*, vol. 64, no. 7, pp. 5907–5918, Jul. 2017.

[11] J. M. Guerrero, J. C. Vasquez, J. Matas, L. G. D. Vicuna, and M. Castilla, "Hierarchical control of droop-controlled AC and DC microgrids—A general approach toward standardization," *IEEE Trans. Ind. Electron.,* vol. 58, no. 1, pp. 158–172, Jan. 2011.

[12] Q. C. Zhong and G. Weiss, "Synchronverters: Inverters that mimic synchronous generators," *IEEE Trans. Ind. Electron.,* vol. 58, no. 4, pp. 1259–1267, Apr. 2011.

[13] S. D'Arco, J. A. Suul, and O. B. Fosso, "A virtual synchronous machine implementation for distributed control of power converters in smartgrids," *Elect. Power Syst. Res.,* vol. 122, pp. 180–197, 2015.

[14] L. Xiong *et al.*, "Static synchronous generator model: A new perspective to investigate dynamic characteristics and stability issues of grid-tied PWM inverter," *IEEE Trans. Power Electron.,* vol. 31, no. 9, pp. 6264–6280, Sep. 2016.

[15] R. Majumder, A. Ghosh, G. Ledwich, and F. Zare, "Angle droop versus frequency droop in a voltage source converter based autonomous microgrid," in *Proc. IEEE PES Gen. Meeting*, Calgary, AB, Canada, 2009, pp. 1–8.

[16] C. Lee, C. Chu, and P. Cheng, "A new droop control method for the autonomous operation of distributed energy resource interface converters," *IEEE Trans. Power Electron.*, vol. 28, no. 4, pp. 1980–1993, Apr. 2013.

[17] J. M. Guerrero, L. G. de Vicuna, J. Matas, M. Castilla, and J. Miret, "A wireless controller to enhance dynamic performance of parallel inverters in distributed generation systems," *IEEE Trans. Power Electron.,* vol. 19, no. 5, pp. 1205–1213, Sep. 2004.

[18] J. M. Guerrero, J. C. Vasquez, J. Matas, M. Castilla, and L. G. .. Vicuna, "Control strategy for flexible microgrid based on parallel line-interactive UPS systems," *IEEE Trans. Ind. Electron.,* vol. 56, no. 3, pp. 726–736, Mar. 2009.

[19] Y. A. I. Mohamed and E. F. El-Saadany, "Adaptive decentralized droop controller to preserve power sharing stability of paralleled inverters in distributed generation microgrids," *IEEE Trans. Power Electron.,* vol. 23, no. 6, pp. 2806–2816, Nov. 2008.

[20] J. Zhou and P. Cheng, "A modified Q-V droop control for accurate reactive power sharing in distributed generation microgrid," in *Proc. IEEE Energy Convers. Congr. Expo.*, Cincinnati, OH, USA, 2017, pp. 4100–4109.

[21] C. Yong, R. Hesse, D. Turschner, and H. P. Beck, "Improving the grid power quality using virtual synchronous machines," in *Proc. Int. Conf. Power Eng., Energy, Electr. Drives*, Malaga, Spain, 2011, pp. 1–6.

[22] J. Liu, Y. Miura, and T. Ise, "Comparison of dynamic characteristics between virtual synchronous generator and droop control in inverter-based distributed generators," *IEEE Trans. Power Electron.*, vol. 31, no. 5, pp. 3600–3611, May 2016.

[23] M. Li, Y. Wang, H. Zhou, and W. Hu, "A phase feedforward based virtual synchronous generator control scheme," in *Proc. IEEE Appl. Power Electron. Conf. Expo.*, San Antonio, TX, USA, 2018, pp. 3314–3318.

[24] X. Meng, J. Liu, and Z. Liu, "A generalized droop control for grid-supporting inverter based on comparison between traditional droop control and virtual synchronous generator control," *IEEE Trans. Power Electron.,* vol. 34, no. 6, pp. 5416–5438, Jun. 2019.

[25] Q. C. Zhong, "Power-electronics-enabled autonomous power systems: Architecture and technical routes," *IEEE Trans. Ind. Electron.*, vol. 64, no. 7, pp. 5907–5918, Jul. 2017.

[26] T. Wu, Z. Liu, J. Liu, S. Wang, and Z. You, "A unified virtual power decoupling method for droop-controlled parallel inverters in microgrids," *IEEE Trans. Power Electron.,* vol. 31, no. 8, pp. 5587–5603, Aug. 2016.

[27] M. Li, Y. Wang, Y. Liu, N. Xu, S. Shu, and W. Lei, "Enhanced power decoupling strategy for virtual synchronous generator," *IEEE Access,* vol. 8, pp. 73601–73613, Apr. 2020.

[28] J. M. Guerrero, L. Garcia De Vicuna, J. Matas, M. Castilla, and J. Miret, "Output impedance design of parallel-connected UPS inverters with wireless load-sharing control," *IEEE Trans. Ind. Electron.,* vol. 52, no. 4, pp. 1126–1135, Aug. 2005.

[29] H. Mahmood, D. Michaelson, and J. Jiang, "Accurate reactive power sharing in an islanded microgrid using adaptive virtual impedances," *IEEE Trans. Power Electron.,* vol. 30, no. 3, pp. 1605–1617, Mar. 2015.

[30] H. Nikkhajoei and R. H. Lasseter, "Distributed generation interface to the CERTS microgrid," *IEEE Trans. Power Del.,* vol. 24, no. 3, pp. 1598–1608, Jul. 2009.

[31] K. D. Brabandere, B. Bolsens, J. V. d. Keybus, A. Woyte, J. Driesen, and R. Belmans, "A voltage and frequency droop control method for parallel inverters," *IEEE Trans. Power Electron.,* vol. 22, no. 4, pp. 1107–1115, Jul. 2007.

[32] Y. Li and L. Y. W. Li, "Power management of inverter interfaced autonomous microgrid based on virtual frequency-voltage frame," *IEEE Trans. Smart Grid*, vol. 2, no. 1, pp. 30–40, Mar. 2011.

[33] X. Yan and Y. Zhang, "Power coupling analysis of inverters based on relative gain method and decoupling control based on feedforward compensation," in *Proc. Int. Conf. Renewable Power Gener.*, Beijing, China, 2015, pp. 1–5.

[34] T. Shintai, Y. Miura, and T. Ise, "Oscillation damping of a distributed generator using a virtual synchronous generator," *IEEE Trans. Power Del.,* vol. 29, no. 2, pp. 668–676, Apr. 2014.
[35] J. Liu, Y. Miura, H. Bevrani, and T. Ise, "Enhanced virtual synchronous generator control for parallel inverters in microgrids," *IEEE Trans. Smart Grid,* vol. 8, no. 5, pp. 1–10, Sep. 2016.
[36] X. Li, Y. Hu, Y. Shao, and G. Chen, "Mechanism analysis and suppression strategies of power oscillation for virtual synchronous generator," in *Proc. 43rd Annu. Conf. IEEE Ind. Electron. Soc.*, Beijing, China, 2017, pp. 4955–4960.
[37] T. Wen, D. Zhu, X. Zou, B. Jiang, L. Peng, and Y. Kang, "Power coupling mechanism analysis and improved decoupling control for virtual synchronous generator," *IEEE Trans. Power Electron.,* vol. 36, no. 3, pp. 3028–3041, Mar. 2021.
[38] B. Li, L. Zhou, X. Yu, C. Zheng, and J. Liu, "Improved power decoupling control strategy based on virtual synchronous generator," *IET Power Electron,* vol. 10, no. 4, pp. 462–470, Jan. 2017.
[39] H. Wu *et al.*, "Small-Signal modeling and parameters design for virtual synchronous generators," *IEEE Trans. Ind. Electron.*, vol. 63, no. 7, pp. 4292–4303, Jul. 2016.
[40] X. Guo, Z. Lu, B. Wang, X. Sun, L. Wang, and J. M. Guerrero, "Dynamic phasors-based modeling and stability analysis of droop-controlled inverters for microgrid applications," *IEEE Trans. Smart Grid*, vol. 5, no. 6, pp. 2980–2987, Nov. 2014.
[41] W. Rui, S. Qiuye, Z. Pinjia, G. Yonghao, Q. Dehao, and W. Peng, "Reduced-order transfer function model of the droop-controlled inverter via Jordan continued-fraction expansion," *IEEE Trans. Energy Convers.*, vol. 35, no. 3, pp. 1585–1595, Sep. 2020.
[42] W. Wu *et al.*, "Sequence impedance modeling and stability comparative analysis of voltage-controlled VSGs and current-controlled VSGs," *IEEE Trans. Ind. Electron.*, vol. 66, no. 8, pp. 6460–6472, Aug. 2019.
[43] Y. Li, Y. Gu, Y. Zhu, A. Junyent-Ferré, X. Xiang, and T. C. Green, "Impedance circuit model of grid-forming inverter: Visualizing control algorithms as circuit elements," *IEEE Trans. Power Electron.*, vol. 36, no. 3, pp. 3377–3395, Mar. 2021.
[44] Y. Li, Y. Gu, and T. C. Green, "Interpreting frame transformations in ac systems as diagonalization of harmonic transfer functions," *IEEE Trans. Circuits Syst. I, Regular Papers,* vol. 67, no. 7, pp. 2481–2491, Jul. 2020.
[45] E. Bristol, "On a new measure of interaction for multivariable process control," *IEEE Trans. Autom. Control,* vol. AC-11, no. 1, pp. 133–134, Jan. 1966.
[46] F. G. Shinskey, *Process Control Systems: Application, Design, and Adjustment,* 3rd ed. New York, NY, USA: McGraw-Hill, 1988, pp. 181–203.
[47] L. Zhang, L. Harnefors, and H. P. Nee, "Power-synchronization control of grid-connected voltage-source converters," *IEEE Trans. Power Syst.,* vol. 25, no. 2, pp. 809–820, May 2010.
[48] M. Li *et al.*, "A novel virtual synchronous generator control strategy based on improved swing equation emulating and power decoupling method," in *Proc. IEEE Energy Convers. Congr. Expo.*, Milwaukee, WI, USA, 2016, pp. 1–7.
[49] Q. Zhong, P. Nguyen, Z. Ma, and W. Sheng, "Self-Synchronized synchronverters: Inverters without a dedicated synchronization unit," *IEEE Trans. Power Electron.*, vol. 29, no. 2, pp. 617–630, Feb. 2014.

**Mingxuan Li** (Member, IEEE) received the B.S. degree from Jilin University, Changchun, China, in 2012, and the Ph.D. degree from the Xi'an Jiaotong University, Xi'an, China, in 2020, both in electrical engineering.

From 2017 to 2019, he was a Visiting Scholar with the Department of Energy Technology, Aalborg University, Aalborg, Denmark. He is currently a Postdoctoral Researcher in control science and engineering with the University of Electronic Science and Technology of China, Chengdu, China. His research interests include distributed power generation systems, microgrids, stability analysis and control of converter-based systems, and artificial intelligence in modern power systems.

**Yue Wang** (Member, IEEE) was born in Liaoning, China, in 1972. He received the B.S. degree from Xi'an Jiaotong University, Xi'an, China, in 1994, the M.S. degree from Beijing Jiaotong University, Beijing, China, in 2000, and the Ph.D. degree from Xi'an Jiaotong University, in 2003, all in electrical engineering.

He is currently a Full Professor with the School of Electrical Engineering, Xi'an Jiaotong University. His research interests include wireless power transfer, active power filters, distributed power generation systems, multilevel converters, and HVdc.

**Weihao Hu** (Senior Member, IEEE) received the B.Eng. and M.Sc. degrees from Xi'an Jiaotong University, Xi'an, China, in 2004 and 2007, respectively, and the Ph.D. degree from Aalborg University, Denmark, in 2012, all in electrical engineering.

He is currently a Full Professor and the Director of Institute of Smart Power and Energy Systems with the University of Electronics Science and Technology of China, Chengdu, China. He was an Associate Professor with the Department of Energy Technology, Aalborg University, and the Vice Program Leader of Wind Power System Research Program with the same department. He has led/participated in more than 15 national and international research projects and he has more than 170 publications in his technical field. His research interests include artificial intelligence in modern power systems and renewable power generation.

Prof. Hu is an Associate Editor for *IET Renewable Power Generation*, a Guest Editor-in-Chief for *Journal of Modern Power Systems and Clean Energy* Special Issue on Applications of Artificial Intelligence in Modern Power Systems, a Guest Editor-in-Chief for Transactions of China Electrical Technology Special Issue on Planning and operation of multiple renewable energy complementary power generation systems, and a Guest Editor for the IEEE TRANSACTIONS ON POWER SYSTEMS Special Section on Enabling very high penetration renewable energy integration into future power systems. He was serving as the Technical Program Chair for IEEE Innovative Smart Grid Technologies Asia 2019 and is serving as the Conference Chair for the Asia Energy and Electrical Engineering Symposium (2020). He is currently a Chair for IEEE Chengdu Section PELS Chapter. He is a Fellow of the Institution of Engineering and Technology, London, U.K.

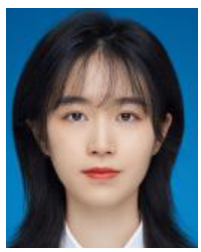

**Sirui Shu** received the B.S. degree in electrical engineering in 2019 from Xi'an Jiaotong University, Xi'an, China, where she is currently working toward the M.S. degree in electrical engineering.

Her research interests include the modeling and control of converter, and renewable energy integration.

**Peng Yu** received the B.S. degree in electrical engineering from Guangxi University, Nanning, China, in 2017. He is currently working toward the M.S. degree in electrical engineering with Xi'an Jiaotong University, Xi'an, China.

His research interests include the modeling and control of converter, and renewable energy integration.

**Zhenyuan Zhang** (Senior Member, IEEE) received the B.S. degree from Chang'an University, Xi'an, China, in 2007, and the Ph.D. degree from the University of Texas at Arlington, Arlington, TX, USA, in 2015, both in electrical engineering.

He is currently a Professor with the School of Mechanical and Electrical Engineering, University of Electronic Science and Technology of China, Chengdu, China. Since 2010, he has been the Project Associate with the IEEE/NFPA Arc Flash Research Project. His research interests include smart grids and arc flash research, but he has also been involved in power system analysis, renewable energy, electrical safety analysis, and power market researches.

**Frede Blaabjerg** (Fellow, IEEE) received the Ph.D. degree in electrical engineering from Aalborg University, Copenhagen, Denmark, in 1995.

He was with ABB-Scandia, Randers, Denmark, from 1987 to 1988. He became an Assistant Professor in 1992, an Associate Professor in 1996, and a Full Professor of power electronics and drives in 1998. In 2017, he became a Villum Investigator. He has authored and coauthored more than 600 journal papers in the fields of power electronics and its applications. He is the Co-Author of four monographs and editor of ten books in power electronics and its applications. His current research interests include power electronics and its applications such as in wind turbines, PV systems, reliability, harmonics, and adjustable speed drives.

Dr. Blaabjerg was the recipient of the 32 IEEE Prize Paper Awards, the IEEE PELS Distinguished Service Award in 2009, the EPE-PEMC Council Award in 2010, the IEEE William E. Newell Power Electronics Award 2014, the Villum Kann Rasmussen Research Award 2014, the Global Energy Prize in 2019, and the 2020 IEEE Edison Medal. He was the Editor-in-Chief of the IEEE TRANSACTIONS ON POWER ELECTRONICS from 2006 to 2012. He has been Distinguished Lecturer for the IEEE Power Electronics Society from 2005 to 2007 and for the IEEE Industry Applications Society from 2010 to 2011 as well as 2017 to 2018. In 2019 and 2020, he was the President of IEEE Power Electronics Society. He is Vice-President of the Danish Academy of Technical Sciences too. He is nominated in 2014–2019 by Thomson Reuters to be between the most 250 cited researchers in Engineering in the world. He is honoris causa with University Politehnica Timisoara, Romania and Tallinn Technical University, Estonia.